COLLAGEN MIMETIC PEPTIDE AS A MARKER OF MECHANICAL DAMAGE IN CEREBRAL ARTERIES

by

Raymond G. Walther

A thesis submitted to the faculty of
The University of Utah
in partial fulfillment of the requirements for the degree of

Master of Science

Department of Mechanical Engineering

The University of Utah

August 2015

The University of Utah Graduate School

STATEMENT OF THESIS APPROVAL

The thesis of **Raymond G. Walther**

has been approved by the following supervisory committee members:

Kenneth L. Monson	, Chair	**14 May 2015** Date Approved
K.L. DeVries	, Member	**14 May 2015** Date Approved
Brittany Coats	, Member	**14 May 2015** Date Approved

and by **Timothy A. Ameel** , Chair/Dean of

the Department/College/School of **Mechanical Engineering**

and by David B. Kieda, Dean of The Graduate School.

ABSTRACT

Traumatic brain injury (TBI) affects an estimated 1.7 million people annually in the United States, 52,000 of whom die as a result of TBI. TBI causes blood vessel dysfunction, and even in cases where hemorrhage is not present, TBI has been linked to long-term effects such as stroke. While vascular dysfunction is understood as a common outcome of TBI, the physiological and biochemical causes of dysfunction are not well understood. Better understanding of the nature of morphological damage to blood vessels will provide guidance in the development of therapies to treat TBI.

This study investigates the effectiveness of collagen mimetic peptide (CMP) as a marker for mechanical damage to cerebral blood vessels exposed to various levels of axial overstretch. Eleven middle cerebral artery (MCA) segments from three lambs were exposed to four levels of axial overstretch. Seventeen sets of confocal images were recorded, with at least one set of images from each vessel. These images were analyzed for four different metrics in an attempt to quantify the difference between control and damaged samples.

Examination of the images showed a number of bright streaks in the adventitia of the damaged samples. It is postulated that these streaks correspond to fibrous, axially oriented collagen structures in the adventitia of the blood vessels. Quantification of the percent of each image above a threshold value showed a significant difference between control samples, and those pulled to failure (p = .0032). This metric was shown to generally increase with increasing local stretch levels. This study shows that CMP is an effective marker for collagen damage due to axial overstretch.

TABLE OF CONTENTS

Chapter

ACKNOWLEDGEMENTS

Thanks are extended to The Royal Society, Taylor and Francis Journals, and Springer publishing for the permission to reuse figures published under their copyright, and to Gary's Meats of Payson, Utah for providing all lamb tissue used in this thesis.

More personal thanks are also due to Matt Converse for his contributions to this study. Matt did the majority of work in brain removals, and performed all dissection and mechanical testing of blood vessels. In addition to his work in the experiments, Matt went above and beyond any reasonable expectation in the number of hours he spent giving guidance, support, and training essential to this study. Without his guidance, and the guidance of Ken Monson, this work would never have been possible.

Also essential to this study were Yang Li and S. Michael Yu. Their group provided all of the collagen mimetic peptide solutions used in this study, as well as the training and guidance necessary to use the solutions for the study.

Finally, this section would be remiss without acknowledgement of the financial and emotional support of Cyane Kramer. In every step of this work, she has been a supportive partner, an intelligent advisor, and a valuable friend.

CHAPTER 1

INTRODUCTION

Traumatic Brain Injury as a Source of Blood Vessel Damage

Traumatic brain injury (TBI) affects an estimated 1.7 million people annually in the United States, 52,000 of whom die as a result of TBI (Faul et al., 2010). TBI is contributing factor in nearly one third of all injury-related deaths in the United States (Faul et al., 2010). Impairment of the cerebral vasculature is a common outcome of TBI, and even in cases where cerebral hemorrhage is not present, TBI has been found to correlate with an increased risk of stroke up to 5 years after the initial injury (Burke et al., 2013; Chen et al., 2011).

Impairment of cerebral vasculature due to TBI has been found to include functional and morphological injury to the cerebral vasculature, leading to decreased blood flow, and disruption of the blood brain barrier (BBB) (DeWitt and Prough, 2003). DeWitt and Prough review a number of studies, in both humans and animals, regarding the response of the cerebral vasculature to TBI (DeWitt and Prough, 2003).

Under normal conditions, the cerebral vasculature is capable of reacting to changes in systemic physiology, such as changes in blood pressure, in order to minimize the effects on cerebral blood flow (CBF). Cerebral arteries are also capable of significant dilation and constriction in response to a number of chemical cues, allowing blood flow responses to a variety of conditions (DeWitt and Prough, 2003).

Following TBI, however, these protective functions are often impaired, contributing to reduced CBF, a significant factor in mortality and morbidity following TBI (Bouma et al., 1991; Bouma et al., 1992b; DeWitt and Prough, 2003; Kelly et al., 1997). In severe clinical cases, reductions in CBF following TBI could become as low as a third of normal (Bouma et al., 1992b), likely resulting in local reductions sufficient to cause neuronal injury in some brain regions (DeWitt and Prough, 2003).

In addition to reduced resting CBF, it has been shown that TBI in humans often results in impairment to the response of cerebral arteries to changes in blood pressure (Bouma and Muizelaar, 1990; Bouma et al., 1992a; Bruce et al., 1973; DeWitt and Prough, 2003; Jünger et al., 1997; Lam et al., 1997; Muizelaar et al., 1984; Munar et al., 2000), as well as reductions in blood CO_2 levels (DeWitt and Prough, 2003; Enevoldsen and Jensen, 1978; Fieschi et al., 1972; Obrist et al., 1984; Overgaard and Tweed, 1974; Suazo et al., 2000). Animal studies have shown impaired responses to changes in blood pressure (DeWitt and Prough, 2003; DeWitt et al., 1992; Engelborghs et al., 2000; Lewelt et al., 1980; Nawashiro et al., 1995; Prat et al., 1997), changes in blood CO_2 (DeWitt and Prough, 2003; Ellis et al., 1991; Lewelt et al., 1982; Wei et al., 1980), hypoxia (DeWitt and Prough, 2003; Lewelt et al., 1982), and hemodilution (DeWitt and Prough, 2003; DeWitt et al., 1996; DeWitt et al., 1997). While many of these impairments appear to heal within days of injury (DeWitt and Prough, 2003), TBI has been correlated with long-term risks of vessel dysfunction, such as stroke (Burke et al., 2013; Chen et al., 2011).

In addition to vessel dysfunction, DeWitt mentions morphological injury and BBB disruption. A variety of animal models showed an opening of the BBB, which began within minutes, and persisted for hours (Baskaya et al., 1997; DeWitt and Prough, 2003; Fukuda et al., 1995; Povlishock et al., 1978; Schmidt and Grady, 1993; Tanno et al., 1992; Whalen et al., 1999). A number of studies (Povlishock and Kontos, 1985; Vaz et al., 1998; Wei et al., 1980), as well as DeWitt's review (DeWitt and Prough, 2003) and a more recent review by Chodobski (Chodobski et al., 2011), implicate morphological injury in the form of damage to the endothelial lining in association with BBB disruption. In addition to these smaller scale disruptions of BBB, hemorrhage is a common outcome of TBI.

While it is understood that the previously described forms of vascular dysfunction are a common outcome of TBI, the causes of dysfunction are not clear. Impairment of vascodilatory and vascoconstrictory responses may be caused by trauma-induced morphological damage to the extracellular matrix (ECM), by changes in the biochemical environment due to injury, or by a combination of the two. Determination of the cause of impairment will provide much needed guidance in development of improved therapies to reduce the effects of TBI. This research investigates direct trauma of cerebral blood vessels, with a focus on damage to the ECM of the vessel wall.

Blood Vessel Microstructure

While the brain makes up only about 2% of the body weight in humans, it receives 15-20% of total cardiac output (Cipolla, 2010). Because of the brain's unique function and structure, it requires not only a high portion of total blood flow, but a fairly constant blood flow (Cipolla, 2010). The ability of the blood vessels in the brain to dilate and contract in order to maintain blood flow, including the ability of cerebral blood vessels to react to chemical cues as well as changes in blood pressure, has been discussed in the previous section. In order to better understand the nature of damage caused by trauma, it is necessary to understand the physical structure of the cerebral blood vessels.

Cerebral arteries are composed of three concentric layers; from interior to exterior they are: the tunica intima, tunica media, and the tunica adventitia (an overview of this structure is shown in Figure 1). The intima is composed of a single layer of endothelial cells, and an internal elastic lamina (IEL). The media is primarily composed of smooth muscle cells, with some elastin and collagen fibers. The adventitia is mostly composed of collagen fibers and fibroblasts, with associated cells for interacting with the surrounding tissue. In contrast to systemic arteries, cerebral arteries lack an external elastic lamina (Cipolla, 2010).

Collagen and elastin fibers compose the majority of the ECM of the cerebral arteries, which carries the majority of mechanical loading (Eble and Niland, 2009). Collagen fibers in the media have been shown to have a nearly circumferential orientation. The adventitial collagen fibers are more axially oriented, with orientation shifting towards more circumferential with higher levels of transmural pressure (Finlay et al., 1998; Wicker et al., 2008). These orientation changes with loading and wall depth are demonstrated in Figure 2. It has also been observed that collagen fibers in the adventitia are generally larger in diameter than those in the media (Wicker et al., 2008).

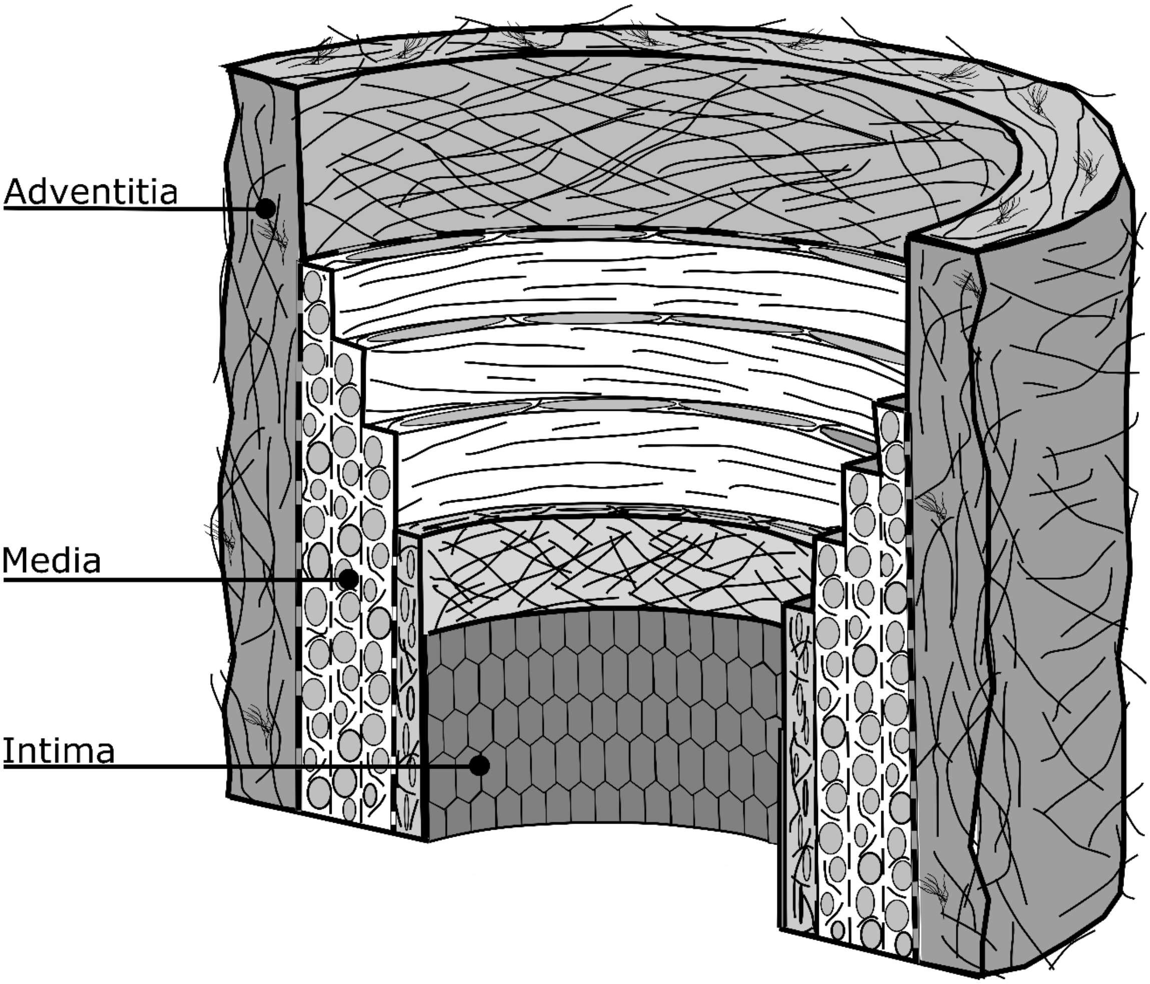

Figure 1. Layers of a blood vessel wall, modified from Holzapfel (Holzapfel et al., 2000).

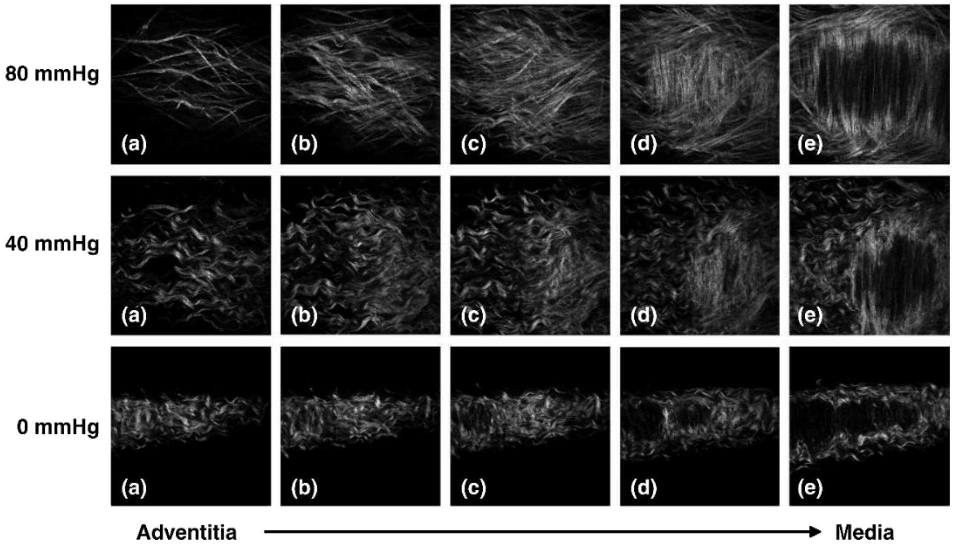

Figure 2. Demonstrative images of fiber orientation change with loading. Images are second harmonic generation (SHG) optical slices from a basilar artery held at 15% extension. Images are oriented so that the horizontal direction is the axial direction of the artery. Note the change in direction of the fibers through the thickness. (Wicker et al., 2008) used with permission.

It can be generally expected that any loading in the axial direction of the blood vessel will primarily be carried by the axially oriented collagen in the adventitia.

Previous Attempts to Image Blood

Vessel Structure and Damage

Previous work in quantifying the interaction between damage and ECM materials (i.e., collagen and elastin) has been primarily dominated by histology methods, both in blood vessels (Austin et al., 2010; Jamal et al., 1992; Ohkawa et al., 1996), and in other tissues (Dodds et al., 2004; Sacks and Schoen, 2002). Electron microscopy has also been previously used to investigate damage in blood vessels (Chan et al., 1995; Jamal et al., 1992; Yamamoto et al., 1992). Histological and electron microscopy methods present the problem, however, of requiring extensive sample preparation. More general investigations of ECM in nonvascular structure have included small angle light scattering (Sacks and Schoen, 2002; Sellaro et al., 2007), and quantifying polarized light microscopy (Quinn et al., 2007; Quinn and Winkelstein, 2008). While these methods offer insight into changes in fiber orientation, however, they do not present a complete look at the fiber arrangement through the entire depth of a tissue sample.

A number of recent works in quantifying the structure of vascular ECM have focused on confocal (Arribas et al., 2007; Rezakhaniha et al., 2012) and multiphoton microscopy (MPM), or nonlinear optical microscopy (NLOM) (Timmins et al., 2010; Wan et al., 2012; Wan et al., 2010; Wicker et al., 2008), because of the ability to image the vessel wall at multiple depths, either in an intact state, with some loading (Arribas et al., 2007; Timmins et al., 2010; Wan et al., 2012; Wan et al., 2010; Wicker et al., 2008), or cut open and laid flat on a slide (Rezakhaniha et al., 2012). The confocal and MPM methods present an advantage over the histological and polarized light methods used by Finlay (Finlay et al., 1995), in that they present essentially the same type of images obtained by use of tangential sectioning, but without the need to cut the vessel and mount multiple samples.

While the confocal and MPM imaging methods have proven useful in quantifying structural changes due to loading, use of these methods alone in an attempt to identify damage after injury could prove prohibitively difficult, requiring extensive imaging at high magnification to find damaged fibers. Recent discoveries of the usefulness of collagen mimetic peptide (CMP) as a marker for denatured collagen suggest that when used with confocal imaging techniques, it may be useful as an alternative means of characterizing collagen damage in cerebral blood vessels.

Collagen Mimetic Peptide as a Marker for Damaged Collagen

CMP is a family of small synthetic peptides that mimic natural collagens, sharing collagen's unique triple helix structure, as well as the Gly-X-Y triplet repeat sequence (Li and Yu, 2013). Traditionally, these peptides have been primarily used to study the structure and folding behaviors of collagen (Engel and Bachinger, 2005). While collagen loses most of its triple helical properties when melted and subsequently cooled, CMPs regain their full triple helical structure, with a slow folding rate (Yu et al., 2011). When unfolded in this manner (i.e., by heating and subsequently cooling), some CMPs showed the ability to bind to collagen films and gels (Yu et al., 2011).

Recent work has shown that CMP can bind to collagen denatured by heat, or by biochemical processes in gels, in vivo, and in tissue samples (Li and Yu, 2013). In vivo studies using systemically delivered CMP conjugated to a near-infrared fluorophore have shown its potential for visualizing regions with high levels of ECM remodeling, such as tumors and joints (Li et al., 2012). When labelled with a fluorescent tag, such as carboxyfluorescein (CF-CMP), CMP has also been shown to bind specifically to collagen in isolated tissue samples (Li et al., 2013).

The affinity of CMP to bind to collagen damaged by heat and biochemical processes suggests that it may be useful as a marker for collagen damaged mechanically. When used in combination with confocal or MPM methods, this marker presents the possibility of visualizing collagen damage in the vessel wall without the need for extensive sample preparation or extensive scanning of the sample.

Objective

Better understanding of mechanical damage to cerebral blood vessels will provide understanding of the mechanisms behind vessel dysfunction following TBI. While methods such as electron microscopy, histology, or NLOM have previously been used to provide insight into the structural and damage behaviors of the vessel wall, none of them are well suited for an in vivo application seeking to understand damage after a TBI model. Histological and electron microscopy methods require extensive sample preparation and slicing, inherently making in vivo implementation difficult or impossible. While NLOM and confocal methods are suitable for imaging intact vessels, an attempt to find ECM damage visible to these methods without the use of CMP would prove work intensive at best.

The demonstrated propensity of CMP to bind to collagen denatured by heat and biochemical processes suggests its usefulness as a marker for collagen which has been damaged mechanically. As a first step toward in vivo implementation, this study seeks to characterize the effectiveness of CMP as a marker for damage due to various levels of axial overstretch in isolated lamb middle cerebral arteries.

CHAPTER 2

METHODS

Axial mechanical damage was produced in lamb middle cerebral arteries (MCAs) following methods similar to previous studies (Bell et al., 2013; Bell et al., 2015; Monson et al., 2008). Samples were then stained in CF-CMP. A portion of the samples were used to investigate the effects of incubation time on the CMP staining. Samples were then imaged using confocal microscopy, and analyzed by a custom Matlab code seeking to quantify high intensity CMP marking. All mechanical testing was performed within 48 hours of animal death, as this is a commonly accepted limit of vessel degradation when testing passive properties (Humphrey, 1995).

Lamb MCAs were selected for this study since they were readily available from the slaughterhouse, relatively large in scale (making them easy to work with), and presented little difference in structure from human cerebral vessels. While adult ewes could have also been used, they were available with far less regularity than lambs.

Dissection and Sample Preparation

The heads of three lambs (specific ages were not known due to the nature of the meat packing plant operation) were obtained from a meat packing plant where they were sacrificed with a humane electrical stunner. As the electrical probes were applied to the brain stem and heart, leaving the MCA relatively far from the direct path of the electricity, it was assumed that the electrical stunning had little effect on the vessels tested. Since unskinned sheep tissue presents a hazard (Q-fever), it was necessary to transport the heads to a facility authorized for the handling of sheep for the removal of brain tissue. The heads were kept on ice during transport.

Within 5 hours of death, the lamb brains were removed from the head, and a slice of tissue surrounding each middle cerebral artery (MCA) was dissected out. The dorsal portion of the skull directly covering the brain was carefully removed by use of a hammer and chisel, taking care not to puncture the brain material. Once the skull material had been removed, the dura mater was carefully dissected using a scalpel. The brain was then carefully removed from the skull, taking care to cut all connections (blood vessels, connective tissue, etc.) without pulling on them. A slice of tissue surrounding each MCA was dissected out, and placed in PBS on ice for transport to the testing facility.

Segments of MCA, each between 4 and 5 mm in length (typical diameter of approximately 1 mm), were dissected from the surrounding tissue, taking care to remove pia-arachnoid tissue. Side branches of the MCA segments were ligated with individual fibrils from unwound 6-0 suture, so as to hold pressure. After dissection, samples were stored in phosphate buffered saline solution (PBS) at 4°C until mechanical testing. Eleven MCA sections were prepared in total.

Mechanical Testing

The mechanical testing of the MCA segments was performed in a manner similar to that described previously (Bell et al., 2013; Monson et al., 2008). Briefly, each segment was cannulated with hypodermic needles, and secured with 6-0 suture and cyanoacrylate glue. In order to allow determination of local stretch values, microspheres were applied to the surface of the blood vessel.

A description of the tester used has been made previously (Bell and Monson, 2013). The needles on which the MCA was mounted were oriented horizontally, in a temperature controlled bath, filled with physiological saline solution (PSS) and maintained at 37°C. The distal needle was held stationary, and mounted to a 250 g capacity load cell (Model 31 Low, Honeywell, Golden Valley, MN) via an X-Y stage (MS-125-XY, Newport, Irvine, CA) that allowed for correction of needle misalignment. The proximal needle was mounted to the tester by a horizontal, low friction sled connected to a voice coil actuator (MGV52-25-1.0, Akribis, Singapore). Position of the actuator was given by a digital encoder (resolution 1.0 µm). Motion of the actuator moved the proximal needle along the sled track, axially stretching the mounted vessel segment. The vessel segment was viewed by use of a digital video camera (PL-A641, Pixelink, Ottawa, Canada) mounted to a light microscope (Ziess 2000C, Carl Zeiss Microscopy, Thornwood, NY) in order to record vessel geometry during testing. The vessel was perfused with warm PSS originating from an open syringe hanging at the appropriate height to provide static fluid pressure. The fluid path passed through the proximal needle, the vessel segment, and the distal needle. Inline pressure transducers

(26PCDFM6G, Honeywell, Golden Valley, MN) were located both proximal and distal to the mounted vessel segment, equidistant from the vessel. The average between these two transducers was taken to be the pressure inside the vessel segment, or the luminal pressure. Data and video acquisition, as well as test setup control, were accomplished by a custom LabView program (National Instruments, Austin, TX).

After mounting the MCA segment, it was preconditioned by oscillating the luminal pressure (6.7-20 kPa) for five cycles while length was held constant at various subfailure axial stretch values. These preconditioning tests were repeated at increasing lengths until the in vivo length (the length at which a change in pressure had a negligible effect on the axial force signal (Van Loon et al., 1977)) was determined. A final pre-conditioning test was performed in which the vessel was held at a length where the needle-to-needle axial stretch was $\lambda_{avg} \approx 1.05$ times in vivo (IV) stretch. Following preconditioning, each noncontrol segment was then subjected to an unpressurized axial stretch test to determine its unloaded, or zero load length (ZLL). Noncontrol samples were subjected to an axial overstretch at one of four needle-to-needle stretch levels (S1: $\lambda_{avg} \approx 1.3$*IV; S2: $\lambda_{avg} \approx 1.4$*IV; S3: $\lambda_{avg} \approx 1.6$*IV; S4: sample pulled axially to failure). Following mechanical testing, vessel segments were carefully removed from the needles in order to prevent further damage, and each was placed in a well of PBS in a 96 well plate. This same 96 well plate was used for all of the staining and rinsing procedures mentioned hereafter.

Vessel Data Processing

Data collected during the mechanical testing were processed to find the ZLL, IV stretch (λ_{IV} referenced to zero load length), needle-to-needle stretch (λ_{avg}), and local stretch levels corresponding with the locations where samples were imaged confocally (λ_{local}). The ZLL was estimated as the length where the axial load began to increase during an unpressurized axial stretch test (Bell et al., 2013).

Stretch values ($\lambda_{avg,}$ λ_{local}) were determined with reference to the IV length. The needle-to-needle stretch was determined for nonfailure samples as the maximum length of the vessel (between the inner edges of the sutures) divided by the IV length of the vessel, as determined by data collected from the linear actuator encoders. The local stretch values were determined by image analysis. The smaller of either the maximum distance between microspheres, or the distance between microspheres just prior to observable failure (where applicable) in the images, was divided by the distance between the same two microspheres in an image where the vessel was held at the in vivo length. As these measurements were taken from the images, care was also taken to watch for large-scale failure of the IEL (defined for the purpose of this study as a circumferentially oriented tear in the IEL which covers the entire circumference of the vessel), which was observable as failure of an inner layer of the vessel prior to loss of pressure, as shown in Figure 3.

Staining

In order to study the effect of staining incubation time, samples from the first two animals were cut in half so as to form two similar cylindrical sections from each

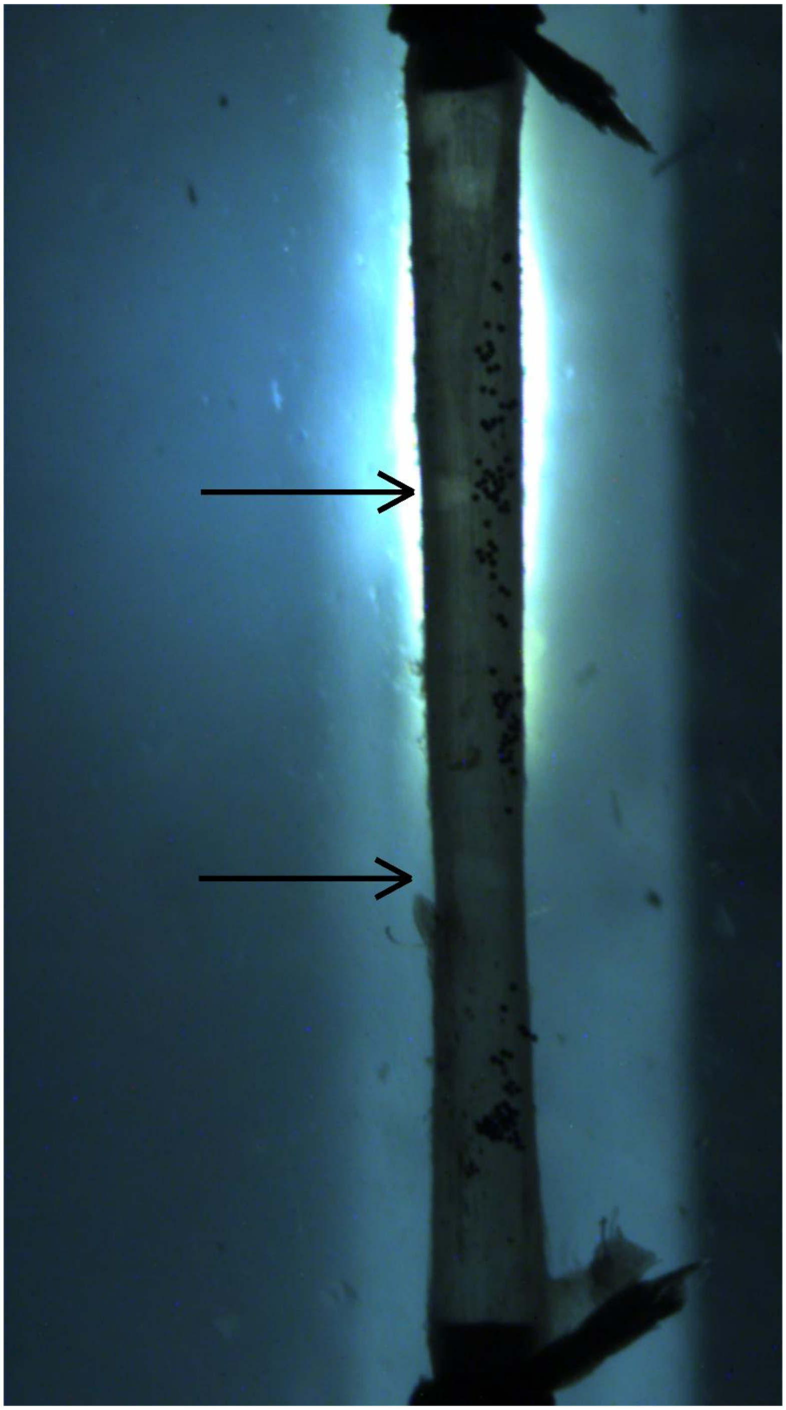

Figure 3. Demonstrative figure showing IEL layer failure (marked by arrows) during mechanical testing. Note that the vessel shown is still holding pressure at this point during testing.

sample. In the case of MCA segments which were pulled to failure, the two failed parts of the vessel were collected, yielding two cylindrical samples similar to those produced by cutting. Samples from the final lamb were left intact, with the exception of samples pulled to failure. In cases where half-samples existed, they were placed in separate wells of PBS following mechanical testing. In all cases, the same 96 well plate used for storage of these samples was used for the subsequent staining and rinsing procedures.

Concurrent with mechanical testing, a PBS solution containing 20 µM of CF-CMP (provided by collaborators in the Michael Yu lab) was prepared, and placed in a vial wrapped in aluminum foil (to prevent light exposure). This vial was placed in a 150 mL water bath on a hot plate set to 70°C. The CF-CMP solution was left in the water bath for 10 minutes, then removed and allowed to cool to room temperature for 5 minutes. After cooling, 90 µL of CF-CMP was pipetted into a well for each half (Animals 1 and 2) or full (Animal 3) segment, and the vessel segments were moved from PBS to the CF-CMP solution, taking care to ensure the vessels were fully submerged. One half of each segment from the first two animals was removed from incubation after 1 hour. With the exception of these half segments, segments were allowed to incubate in the CF-CMP solution for 18 hours ("overnight"). During incubation, the well plate was wrapped in aluminum foil to prevent light exposure, and stored at 4°C.

At the end of the incubation period, each segment was moved to a well filled with 300 µL PBS, and the well plate was wrapped in foil to prevent light exposure. The foil wrapped plate was placed on a shaker for 10 minutes to rinse the vessels. This rinsing procedure was repeated three times, for a total of 30 minutes rinsing time. After rinsing, the segments were cut open by slicing the sidewalls lengthwise with scissors. Once each segment was cut open, it was laid flat on a glass slide, with the lumen side down. The segments were then covered with fluoromount, and a coverslip was placed on top.

Microscopy

An overview of each segment was first obtained by fluorescence imaging at 4x magnification on an upright microscope (Eclipse E600, Nikon Instruments, Melville, NY) with a mercury bulb. Images were recorded using a 2-second exposure time. For simplicity, confocal stacks were only taken of samples incubated overnight. Each sample incubated overnight was then imaged at 10x on an Olympus confocal microscope (Model BX61WI, Olympus Scientific Solutions, Waltham, MA) using Olympus FluoView Software (Olympus Scientific Solutions, Waltham, MA). Confocal stacks were taken with a step size of 2 µm from the luminal wall (defined as the slice 6 µm to the luminal side of where the internal elastic lamina was in focus) to the exterior edge of the vessel wall (defined as the slice where adventitial features reached peak brightness). Stacks were taken side by side so as to obtain an image strip covering the full circumference of the vessel, as diagrammed in Figure 4. For each stack, data were collected from the green (AlexaFluor 488; HV: 550; Gain: 1; Offset: 6) channel to show CF-CMP fluorescence, as well as the blue (AlexaFluor 405; HV:550; Gain:1; Offset: 6) channel, since this channel allowed visualization of the IEL. In general, an effort was made to avoid imaging within a field of view of the suture sites or the failed edges of cut samples.

Since MCA segments from the first two animals were cut in half, it was only

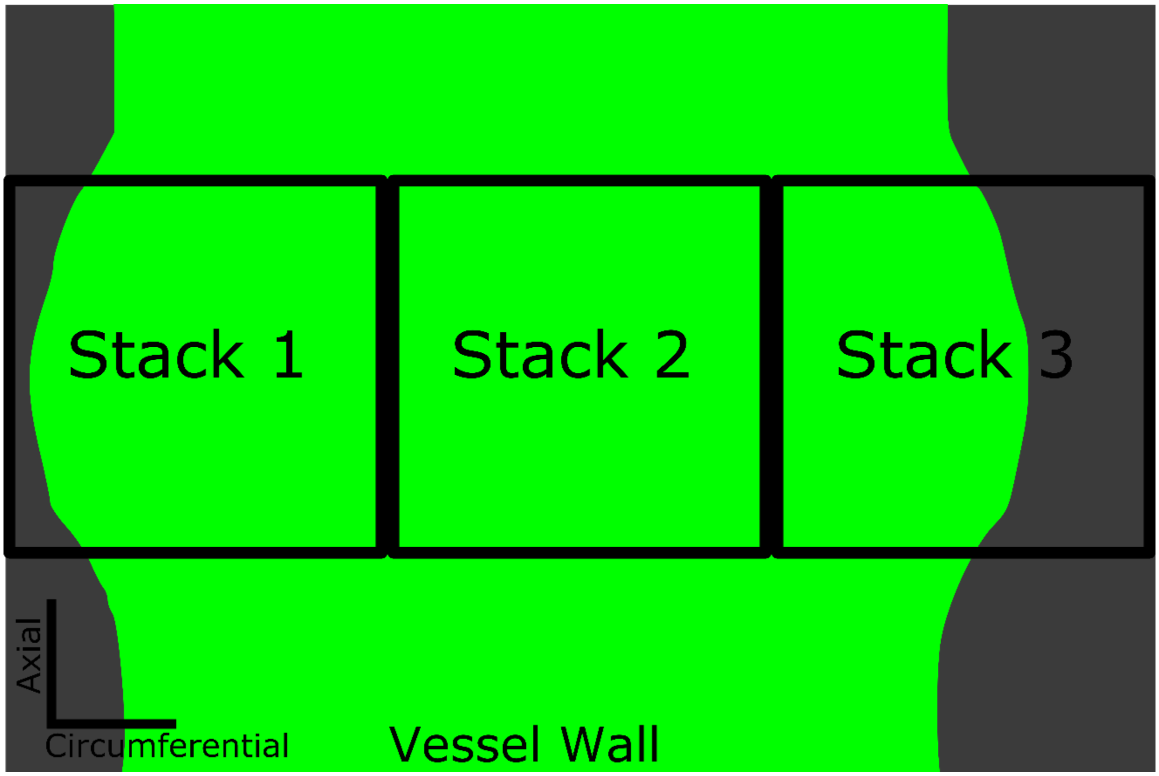

Figure 4. Diagram of how image stacks were taken so as to obtain an image strip of the full vessel circumference. Image is demonstrative, and not intended to represent any specific scale.

possible to obtain one image strip from each 18-hour segment. Segments from the third animal, however, were of full length, so that two or three image strips could be obtained from each. Each of these strips was treated separately when performing image analysis, rather than stitching them together to obtain a single, larger stack.

Image Analysis

Side by side stacks were stitched together using a custom Matlab script (included in the Appendix) to form stacks covering the full vessel circumference. These stacks were then masked in order to remove background pixels on either side of the vessel, and confounding structures such as microspheres, branches, and sutures. This masking was accomplished by first removing all pixels below a user-defined background threshold. Other structures were then removed by user-defined areas, drawn directly on an image from the stack. This masking allowed for metrics to be normalized by the number of usable pixels in the image, rather than the full number of pixels.

After masking, the stacks were analyzed using a custom Matlab code (included in the Appendix) to find the maximum pixel brightness in each image, the average pixel brightness in each image, the number of “bright pixels”, and the number of lines in the image, as found by the Hough transform. The number of bright pixels was defined as the number of pixels in an image which exceeded 2.0 times a control value. The control value used for each vessel was the average brightness of the brightest image from the control sample from the same animal and staining batch (i.e., if the average brightness of images from a control sample was plotted as in Figure 5, the control value would be the peak of the curve shown). In order to account for variations in wall thickness, metrics were plotted as a function of normalized wall depth (defined as the current depth divided by the maximum wall depth, or thickness).

Statistical Analysis

Results of the metrics outlined above were analyzed for statistical significance by splitting the results into three groups: controls, subfailure damage (S1, S2, and S3), and failure damage (S4). For each metric tested, a single value per sample was first determined. For the maximum pixel brightness metric, the average across all images was used; for the number of lines found by the Hough transform, the average value

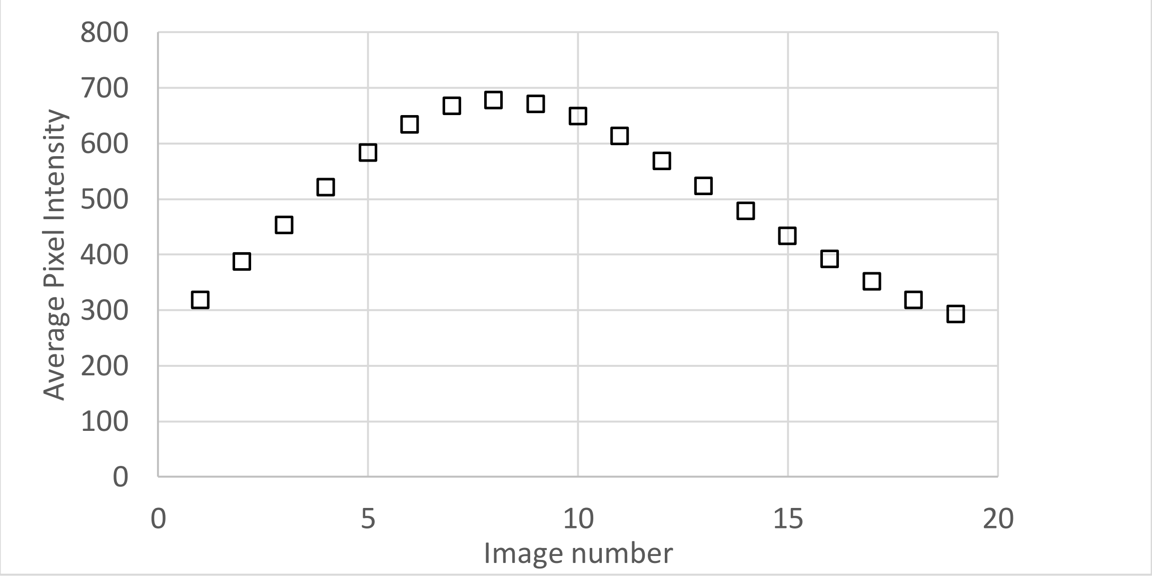

Figure 5. Demonstrative image of control value determination for use in bright pixel metric. The control value used in determination of bright pixels is the same as the maximum of the data shown. Data are from a control sample from this study.

across all images was used. For the average pixel brightness, and percent bright pixels metrics, the peak values (i.e., the value from the image with the highest average pixel brightness, and the value from the image with the highest percent bright pixels) were used. A Levine test was performed based on the medians, in order to determine if the variances in the group were similar. In cases where the variances were similar (p-values from the Levine test of more than .05), ANOVA was used to determine if a significant difference in means between the groups existed (p-values from ANOVA less than .05). Where appropriate, t-tests were then performed to compare the groups. Where the Levine test showed ANOVA was not suitable (p-values less than .05), Welch's ANOVA was used, and, as appropriate, a Games-Howell test was used to check for statistical differences between groups.

CHAPTER 3

RESULTS

Eleven vessel segments in total were tested. Multiple image sets were taken of samples from the final animal, resulting in seventeen image sets total. Table 1 presents a summary of these results by animal, including the label applied to each image set, as well as the needle-to-needle stretch the vessel experienced, and a measure of the local stretch in the region where confocal images were taken. In the case of Vessel 1 from Animal 3 (S4_6, S4_7, S4_8), the numerous occurrences of IEL failure during testing, as well as the distribution of microspheres on the vessel, made local measures of stretch for each image set vary widely. Results are presented, therefore, for a measurement encompassing all three imaging regions.

Incubation Time Study

Fluorescence microscopy images of incubation time study samples from the first and second animals are shown in Figure 6 and Figure 7, respectively. All of the images in the figures were taken at 4x magnification with a 2-second exposure time; the images are oriented so that vertical and horizontal correspond to the axial and circumferential directions, respectively. Note the significant difference in sample brightness between the 1-hour and overnight images, making the samples incubated for a shorter duration

Table 1. Summary of results. ZLL is the zero load length, determined from an unpressurized axial stretch test. λ_{IV} is the axial stretch (referenced to the ZLL) at the in vivo length. λ_{avg} is the needle-to-needle stretch (referenced to the in vivo length), determined from actuator measurements. λ_{local} is the stretch level (referenced to the in vivo length) in the region imaged, as determined from measurement of microspheres in the test video. Vessel 3 of Animal 1 and Vessel 4 of Animal 2 (marked with ‘*’) were overstretched multiple times prior to the final overstretch test. Values of λ_{local} for Vessel 1 of Animal 3 (marked with ‘†’) were obtained by a single microsphere measurement over the full imaged area, due to the distribution of microspheres and multiple IEL failures in the area of interest.

Animal	Vessel	ZLL	λIV	λavg	λlocal	Label
1	1	--	--	1.05	--	C1
	2	4.51	1.23	1.60	1.35	S4_1
	3*	3.12	1.17	Failure	1.73	S4_2
2	1	5.19	1.1	1.30	1.23	S1_1
	2	--	--	1.05	--	C2
	3	3.64	1.16	1.40	1.19	S2_1
	4*	3.59	1.14	1.63	1.36	S3_1
3	1†	4.76	1.16	Failure	1.35	S4_6
					1.35	S4_7
					1.35	S4_8
	2	5.6	1.13	Failure	1.34	S4_3
					1.47	S4_4
					1.43	S4_5
	3	4.29	1.23	1.40	1.29	S2_2
					1.45	S2_3
	4	--	--	1.05	--	C3
					--	C4

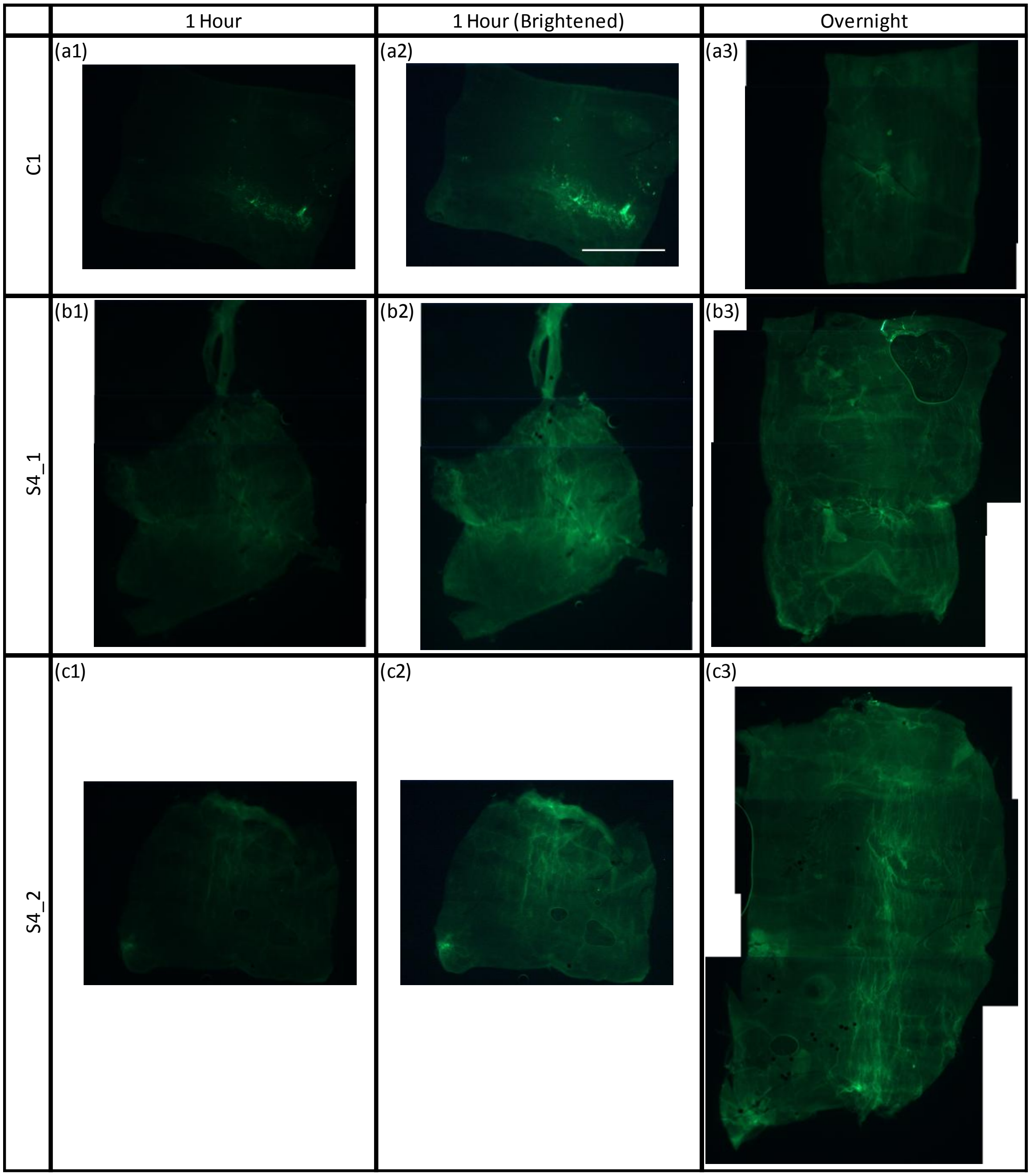

Figure 6. Fluorescence images of time study samples from Animal 1. The brightened 1-hour images (a2, b2, c2) were brightened by displaying only pixels between 0 and 100, so that bright spots showed close to the same level of fluorescence as bright spots in the overnight samples (a3, b3, c3). The scale bar in the brightened image of C1 (a2) is equivalent to 1 mm.

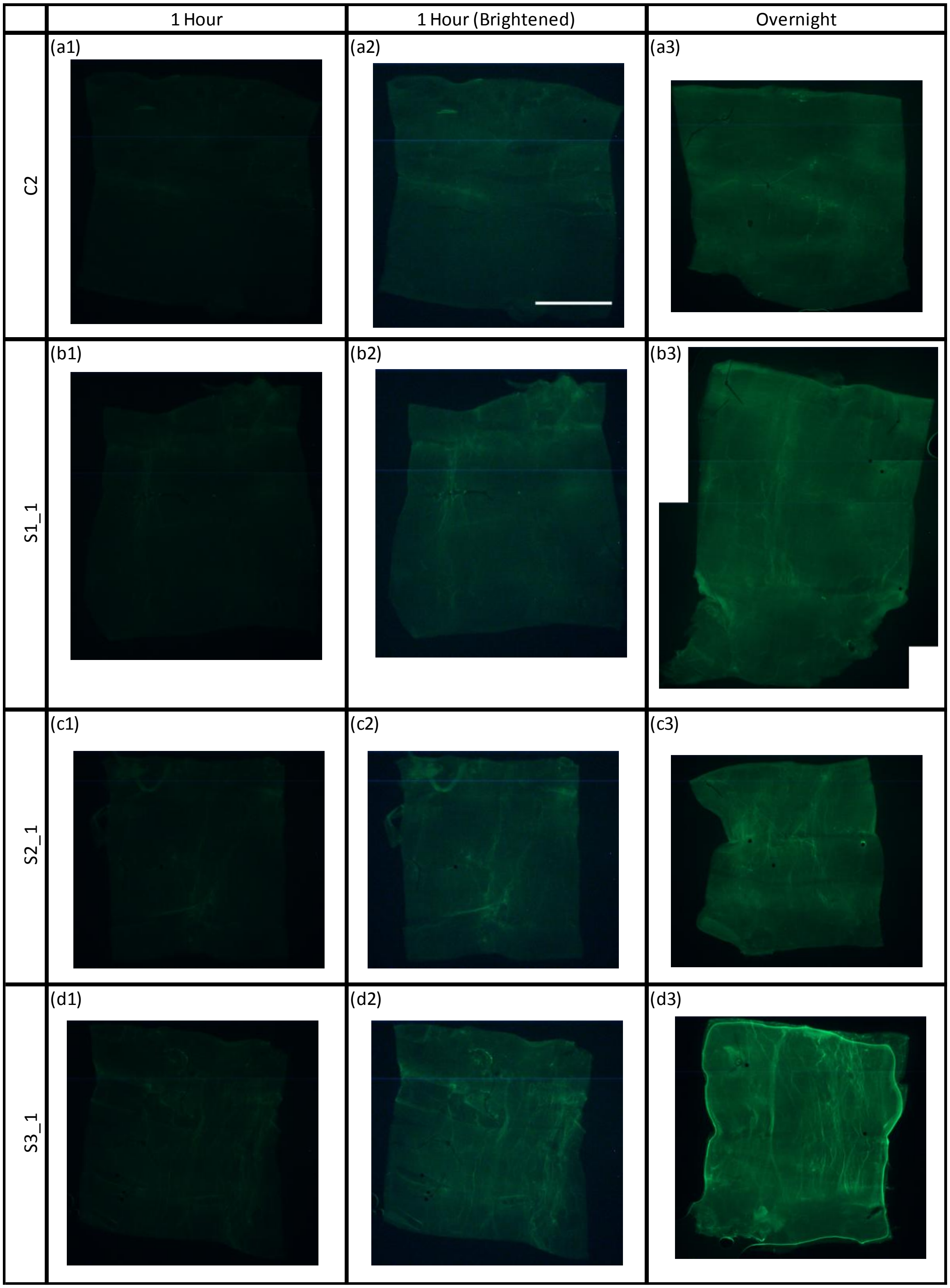

Figure 7. Fluorescence images of time study samples from Animal 2. Images of 1-hour samples were brightened in the same manner as in Figure 6. The scale bar in the brightened image of C2 (a2) is equivalent to 1 mm.

more difficult to interpret. After the images were manually brightened, however, the 1-hour samples showed features similar to the overnight samples.

While no formal quantification of these images was performed, in order to compare the brightened images to the overnight samples, a simple analysis of pixel values was performed. A pixel from one of the bright streaks in each of the damage samples of Animal 1 was evaluated to get red, green, and blue (RGB) values. A pixel from another “background” section of the vessel was then evaluated to get its RGB values. It was found in this comparison that red values for all pixels sampled were very low (less than 7). Green values for background pixels tended to be similar between both groups (between 40 and 60). These pixels in the brightened images showed somewhat higher blue values (35 compared to between 16 and 24). The green values from the bright features differed, however, with brightened images giving values around 120, and the overnight images giving values between 160 and 200. Taking the ratio of green values between bright streak pixels and corresponding background images gave values of 4.95 and 3.03 for the overnight images, compared to 2.5 and 2.65 for the brightened images. This suggests that while the features shown in both images are similar, the background pixels in the brightened images are much closer in brightness to the bright streaks. This suggests that while staining has begun at 1 hour, at 18 hours, there is a better chance of staining showing a difference between background pixels and the features visualized as bright streaks in the fluorescence images.

Damage Study

Qualitative Image Analysis

The damage study was conducted using samples stained overnight, so that all samples shown hereafter are from overnight incubations. Fluorescence images of each sample are presented by animal in Figure 8, Figure 9, and Figure 10 (i.e., Figure 8 shows samples from Animal 1, Figure 9 from Animal 2, and Figure 10 from Animal 3). The images consistently show a number of bright, axially oriented streaks in samples pulled to the two most extreme stretch levels (S3 and S4, λ_{avg} between 1.6 and failure level), and an absence of such streaks in control samples. Lower stretch level (λ_{avg} from 1.3-1.4) samples show some evidence of streaks similar to those in the S3 and S4 (λ_{avg} from 1.6 to failure) samples, but there appear to be fewer streaks, and they appear to be less bright. All of these observations were made qualitatively, as fluorescence images were intended to be used only as an overview to inform the confocal imaging and analysis process.

Stitched confocal image stacks from the samples were first analyzed qualitatively by direct observation. Demonstrative images from the green (CMP staining) channel of each stack are shown in Figure 11, Figure 12, and Figure 13. These figures are organized by animal (i.e., Figure 11 shows images from the first animal, Figure 12 from the second, and Figure 13 from the third). All images in these figures were adjusted to show pixels with intensity values between 42 and 4079, so that brightness could be compared directly between images. Images were selected by use of the normalized wall thickness parameter defined in the Methods section. The inner media images were defined as the

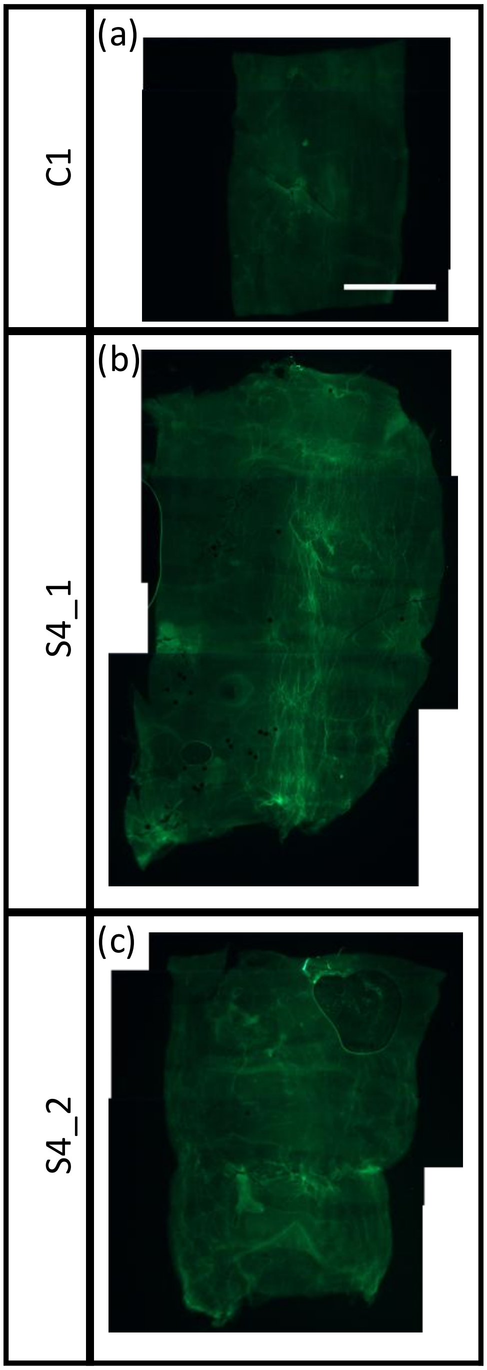

Figure 8. Fluorescence images of samples from Animal 1. (a) control. (b) and (c) S4 (pulled to failure) samples. The scale bar in the image of C1 (a) is equivalent to 1 mm.

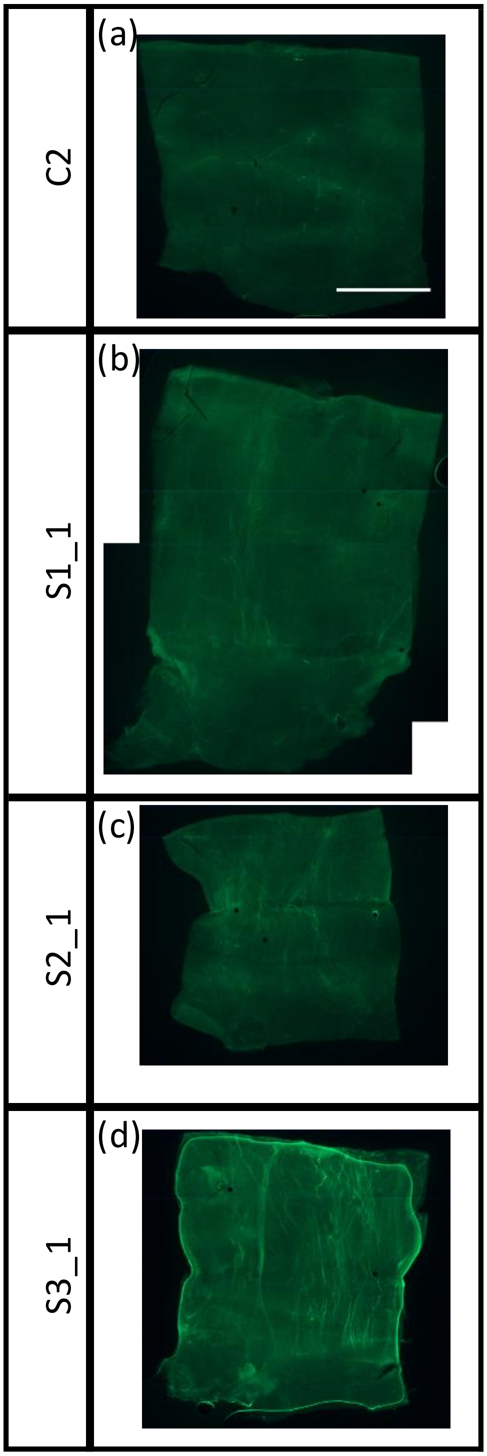

Figure 9. Fluorescence images of samples from Animal 2. (a) control. (b) S1_1 (λavg ≈ 1.3*IV). (c) S2_1 (λavg ≈ 1.4*IV). (d) S3_1 (λavg ≈ 1.6*IV). The scale bar in (a) is equivalent to 1 mm.

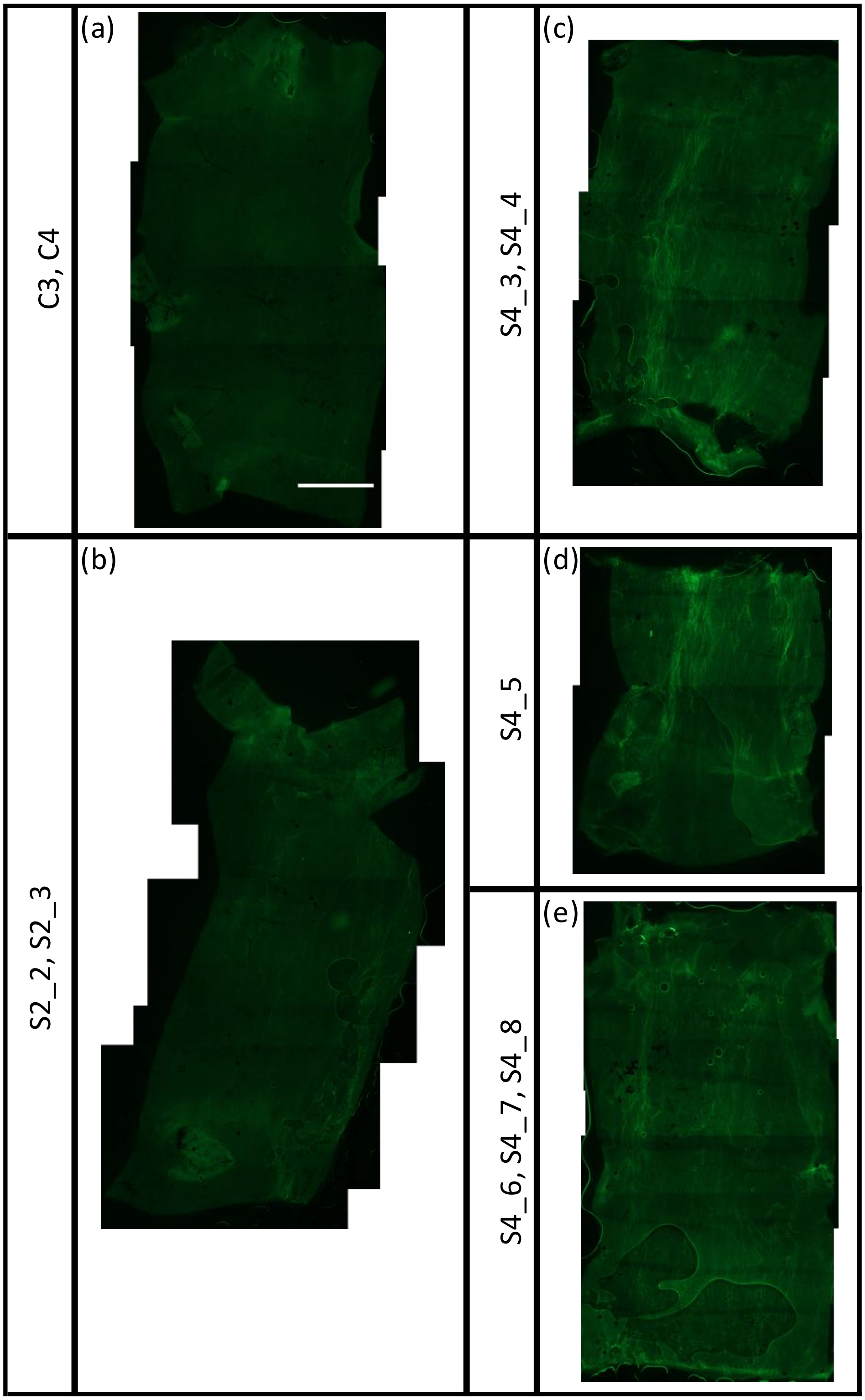

Figure 10. Fluorescence images of samples from Animal 3. (a) control. (b) S2_2, S2_3 (λavg ≈ 1.4*IV). (c, d, e) S4 (samples pulled to failure). The scale bar in (a) is equivalent to 1 mm.

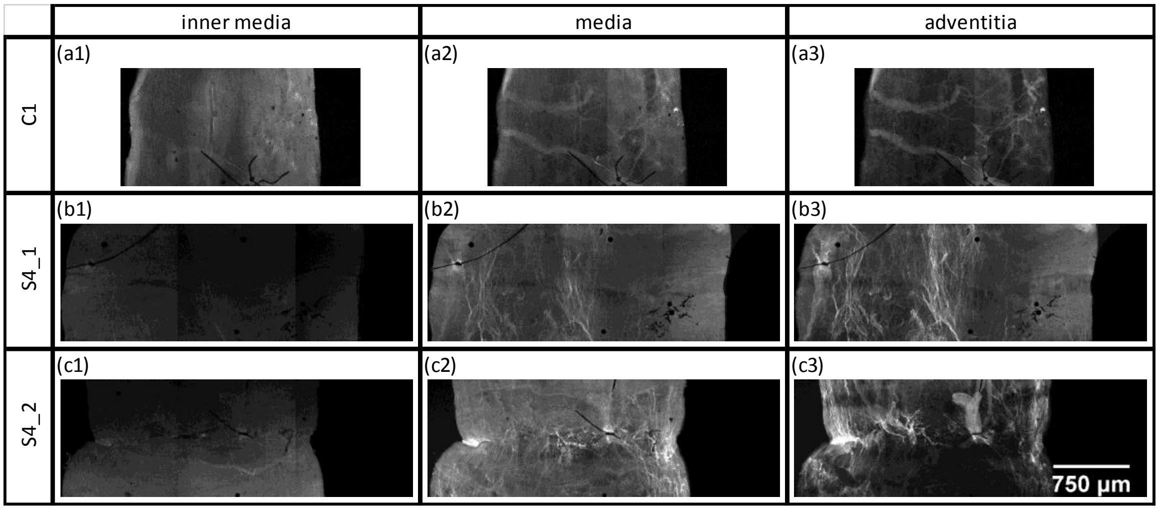

Figure 11. Green channel (CMP) confocal images of samples from Animal 1. Images are oriented so that the horizontal and vertical directions correspond with the axial and circumferential directions, respectively. Inner media was defined as the image closest to 5 percent through the normalized thickness; media was defined as the image closest to 50 percent through the thickness; adventitia was defined as the image closest to 75 percent. (a1, a2, a3) control sample. (b1, b2, b3) S4_1 (λlocal = 1.35), and (c1, c2, c3) S4_2 (λlocal = 1.73), both of which were pulled to failure.

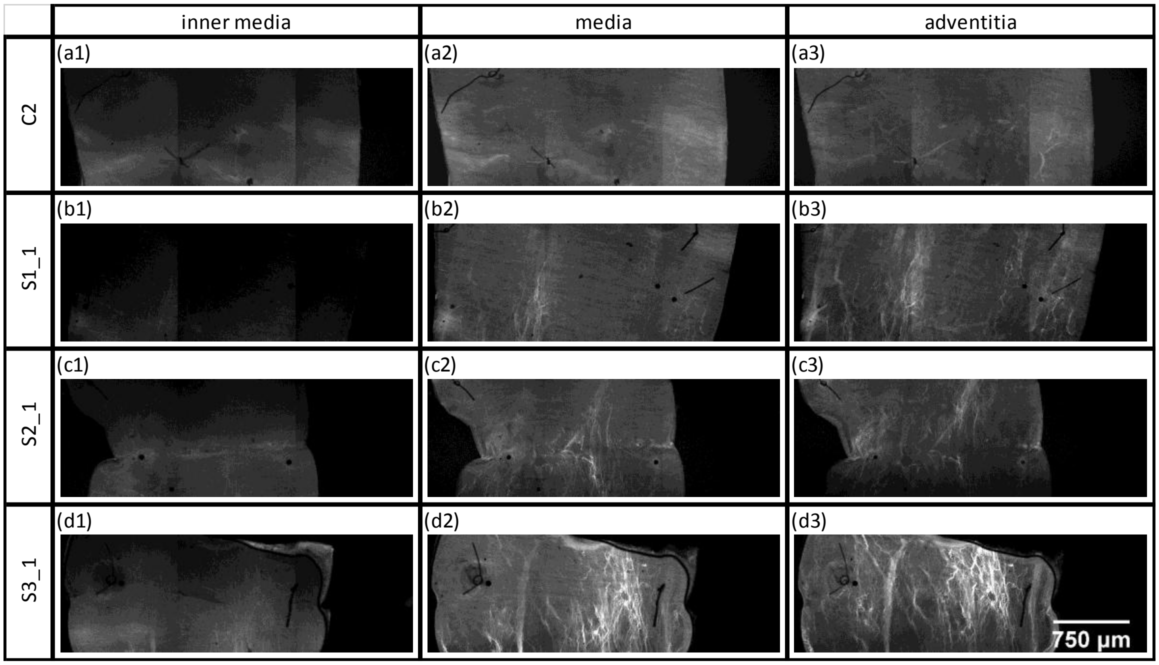

Figure 12. Green channel (CMP) confocal images of samples from Animal 2. The images are organized in the same manner as in Figure 11; that is, (a1, a2, a3) control sample, with the other samples in ascending order from low stretch level to high stretch level.

Figure 13. Green channel (CMP) confocal images of samples from Animal 3. (a1-3, b1-3) two sets of images from the same control sample. Images from S2_2 (c1-3) and S2_3 (d1-3) are from two sets of images of the same vessel segment. The remainder of samples were from failure level samples. Images labelled S4_3 (e1-3), S4_4 (f1-3), and S4_5 (g1-3) were from the same segment. S4_6 (h1-3), S4_7 (i1-3), and S4_8 (j1-3) were also taken from the same segment.

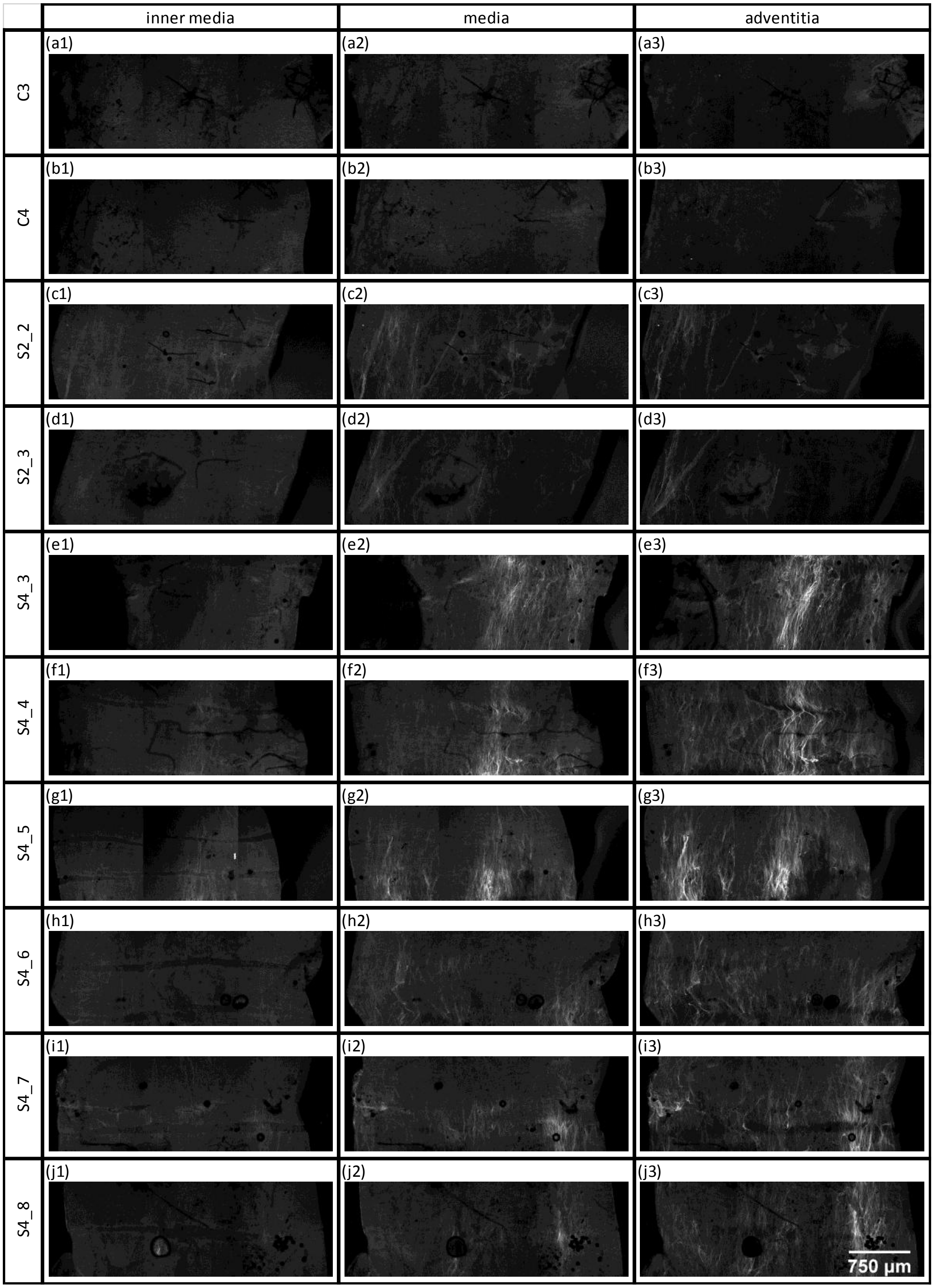
inner media
media
adventitia
C3
(a1)
(a2)
(a3)
C4
(b1)
(b2)
(b3)
S2_2
(c1)
(c2)
(c3)
S2_3
(d1)
(d2)
(d3)
S4_3
(e1)
(e2)
(e3)
S4_4
(f1)
(f2)
(f3)
S4_5
(g1)
(g2)
(g3)
S4_6
(h1)
(h2)
(h3)
S4_7
(i1)
(i2)
(i3)
S4_8
(j1)
(j2)
(j3)
750 µm

image closest to 5 percent through the thickness, the media images as the slice closest to 50 percent, and the adventitia images as the slice closest to 75 percent. Vessel wall thickness, as found from the confocal stacks, ranged from 22 µm to 42 µm.

Examination of these figures shows that in all cases, images from the media and adventitia of noncontrol images exhibit bright, streak-like features oriented in the axial direction. The intensity and density of these streaks appears to increase sharply in moving from the S2 level ($\lambda_{avg} = 1.40$) samples to the S3 ($\lambda_{avg} = 1.63$) and S4 (sample pulled to failure) level samples. The axial orientation of these streaks, as well as the fact that their brightness appears to peak in the outer media or adventitia of the vessel wall, suggests that CMP is binding to damage sites on large, axially oriented fibers in the adventitia. While these features are visible in the media, this is likely due to the large optical section thickness (the thickness through depth of an image taken by the confocal scope; 10.66 µm at 10x magnification) of the confocal setup used, which was close to half the wall thickness for the thinnest samples imaged. Since collagen in the media has previously been shown to be primarily helically oriented, it is unlikely that it would be severely damaged during an axial stretch event.

It is also worth noting that the samples from the third animal were significantly less bright than those from the other animals. This difference was accounted for in the later counting of bright pixels by use of a control value determined from the control vessel associated with each animal.

Examination of both fluorescent images and confocal images also showed some correlation between the target stretch level and the presence of large-scale failure of the IEL. While IEL tearing was present in virtually all samples at the sites where vessels were tied down using suture, control samples showed no large-scale IEL failure between suture sites in mechanical testing video, or in the fluorescence images. With the exception of C1, blue channel confocal images of the control samples (shown in Figure 14) showed no IEL tears larger than one third of the diameter of any control sample. Given that the large IEL tears present in C1 are oriented axially rather than circumferentially, it is unlikely that they are due to the mechanical testing procedure. It is possible that they occurred due to the process of laying the vessel flat on the slide.

Demonstrative blue channel IEL images of the damaged samples are shown in Figure 15 and Figure 16. Figure 15 shows images from all S1, S2, and S3 samples. While the majority of these samples showed IEL damage comparable with the control levels, S2_1 had one instance of large-scale IEL failure, which was visible both in mechanical testing video and in fluorescence images of the sample. The other sample stretched to the same level did not exhibit the same level of IEL failure, suggesting that the S2-S3 (λ_{avg} = 1.4-1.6; λ_{local} = 1.19-1.36) stretch level is near the threshold for large-scale IEL failure.

Due to the large number of S4 images, demonstrative images only are presented in Figure 16. In every S4 sample, multiple instances of significant IEL failure were present and were visible in the mechanical testing video and in fluorescence imaging.

Quantification

All confocal images were evaluated to determine four metrics. Images were first analyzed to determine the average pixel brightness value, as the maximum value of this

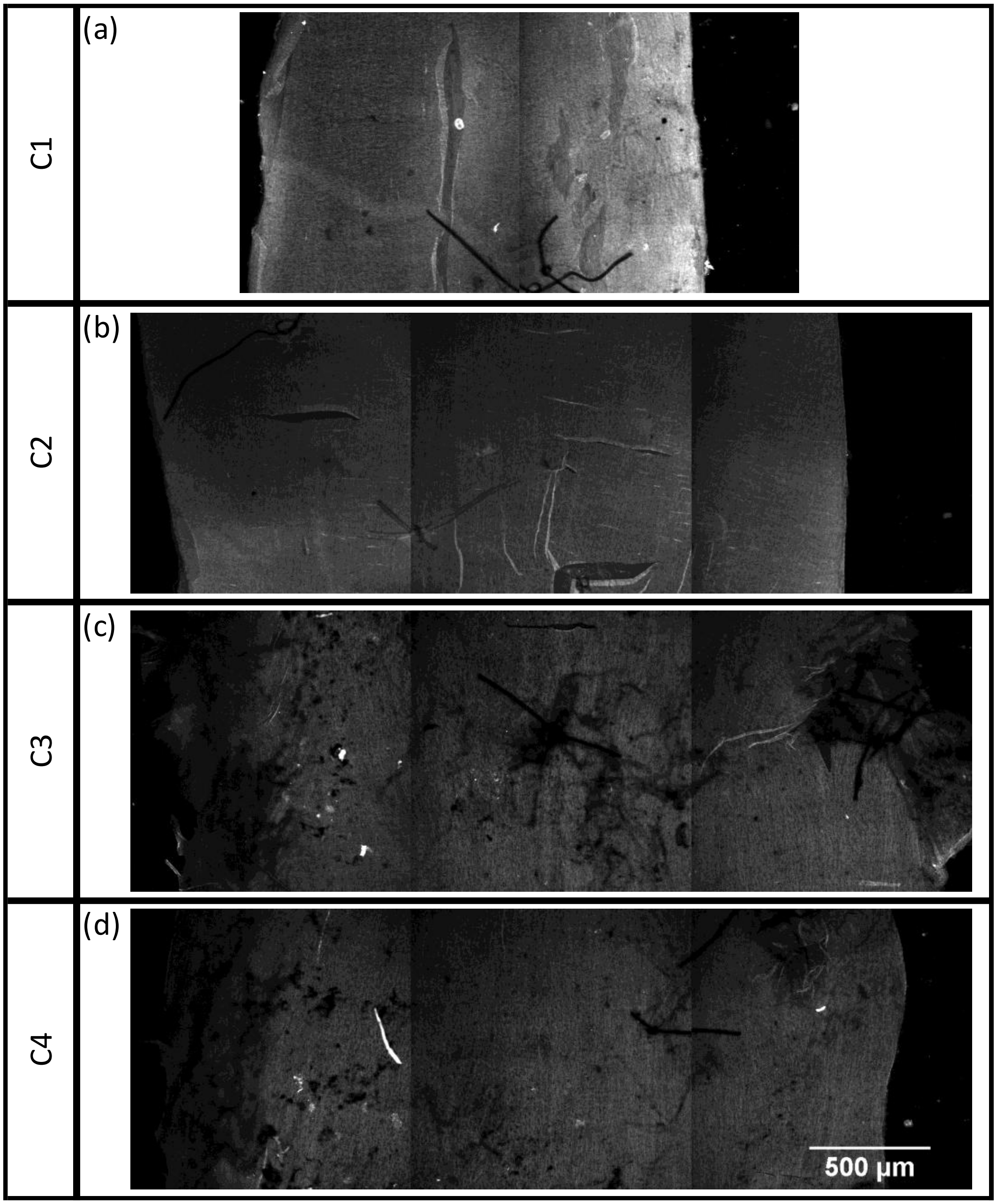

Figure 14. Blue channel IEL images of control samples. (a) Animal 1, (b) Animal 2, (c) and (d) Animal 3

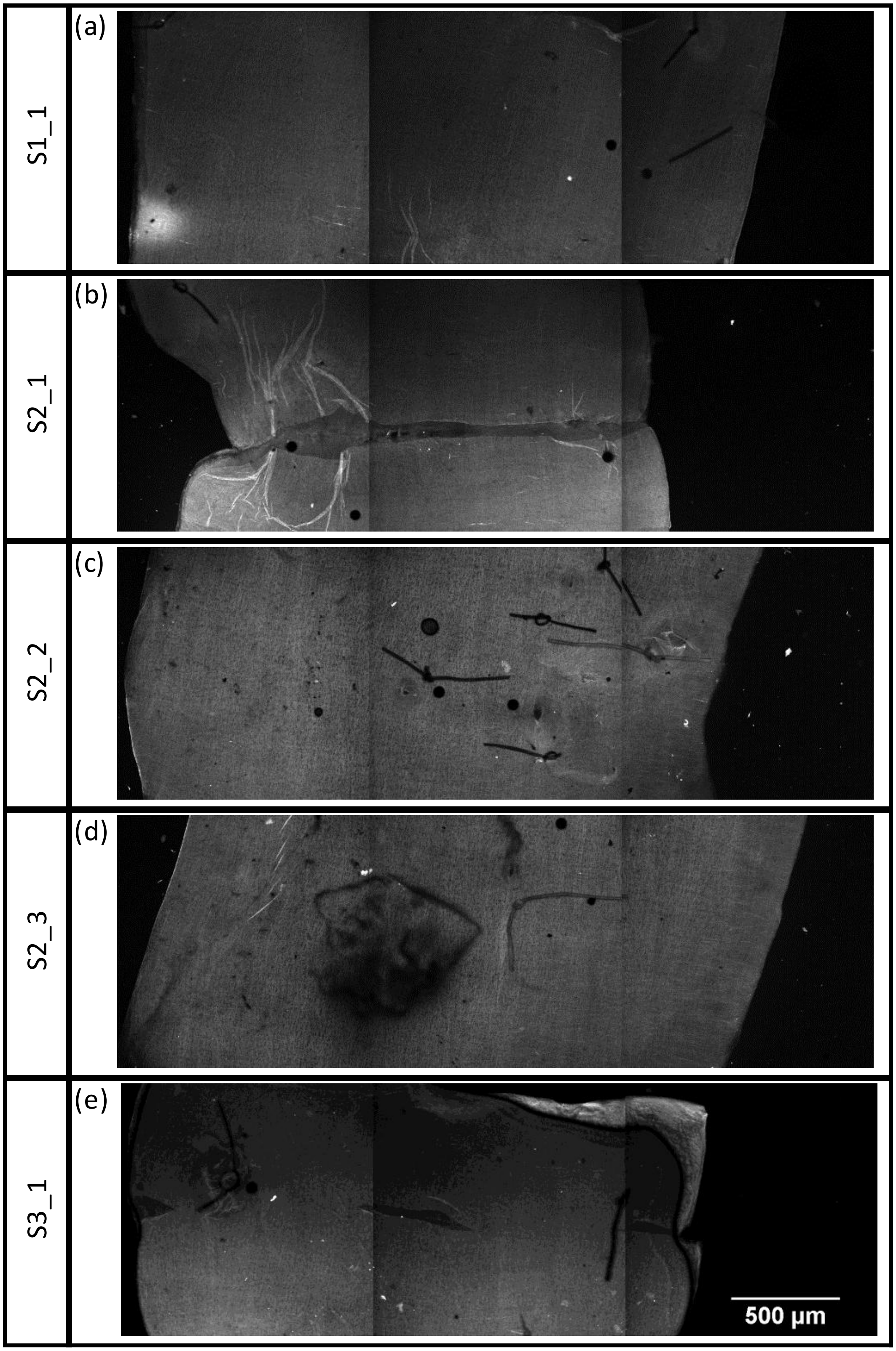

Figure 15. Blue channel IEL images of S1, S2, and S3 samples.

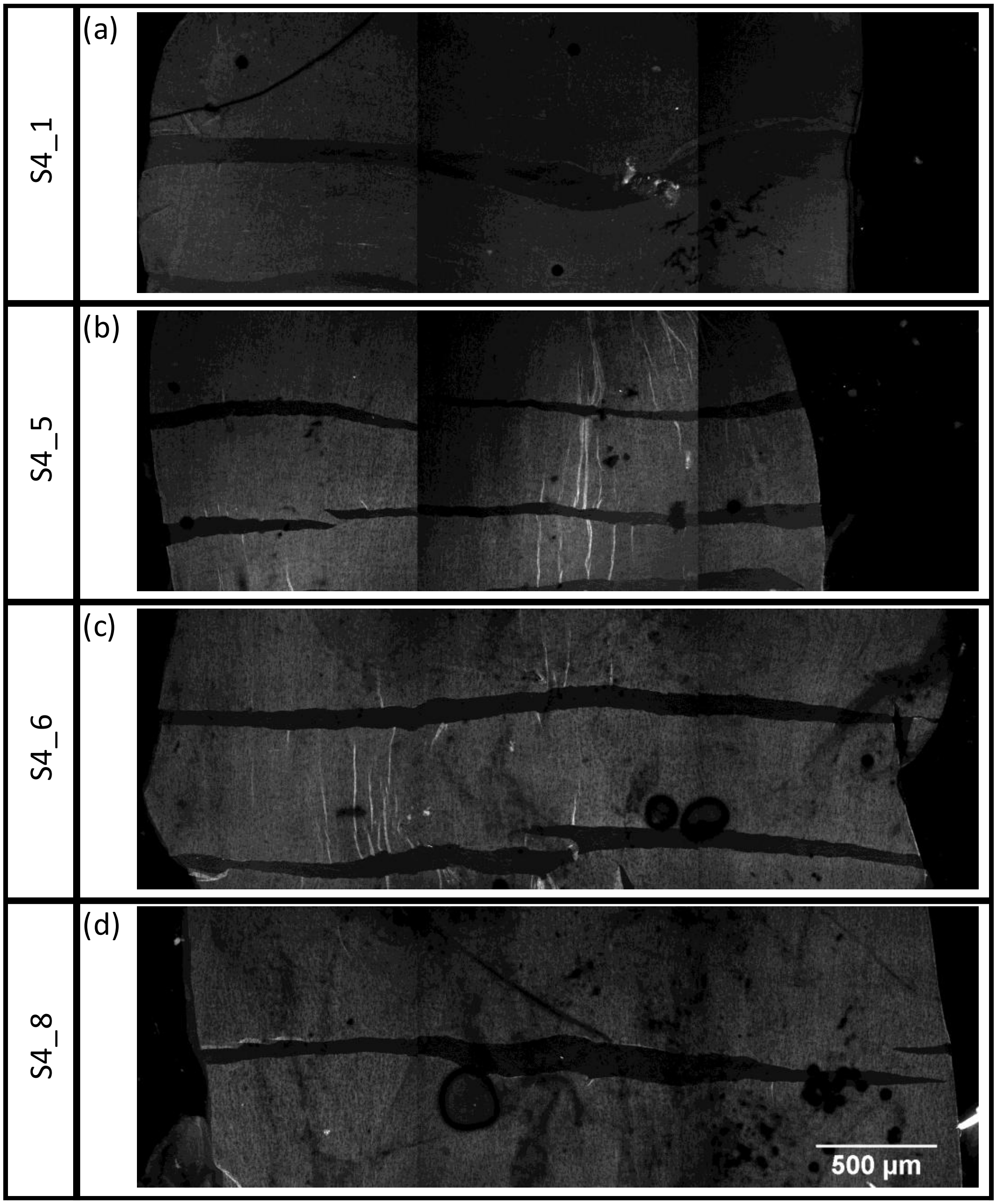

Figure 16. Demonstrative blue channel IEL images of S4 level samples

metric for each control was used in determining the percent of the image that was composed of bright pixels. After the average pixel values were evaluated, three other metrics were also evaluated: the maximum pixel intensity, the percent bright pixels, and the number of lines found by the Hough transform.

Prior to analysis for other metrics, it was necessary to find the average pixel brightness for each confocal image of each sample. This metric was analyzed for two reasons: firstly, it was analyzed to determine if damage to the samples caused an increase in the overall brightness of the images; secondly, the average brightness values from the control sample of each animal were used as a means of normalizing for variation between samples. This metric proved to be have a similar distribution through the wall thickness for all samples, following a parabolic or bell curve as demonstrated by the values for samples from Animal 2, shown in Figure 17. For simplicity, only the peak values (i.e., the maxima of the curves from Figure 17) are presented in Figure 18 and Figure 19. Because the magnitudes of the control values for the first two animals were so similar (as shown in Figure 18), an average of the peaks of C1 and C2 was used in the final quantification of the percent bright pixels for samples from the first two animals. An average of C3 and C4 was used in the bright pixel quantification of the third animal.

Figure 19 shows the peak values of average intensity, split by animal. Aside from the large decrease in peak brightness of samples from the third animal as compared to the first two, little difference between samples was observed for this metric. ANOVA comparison of the peak values of the average brightness curve showed no significant difference between the control, subfailure, and failure damage groups, whether

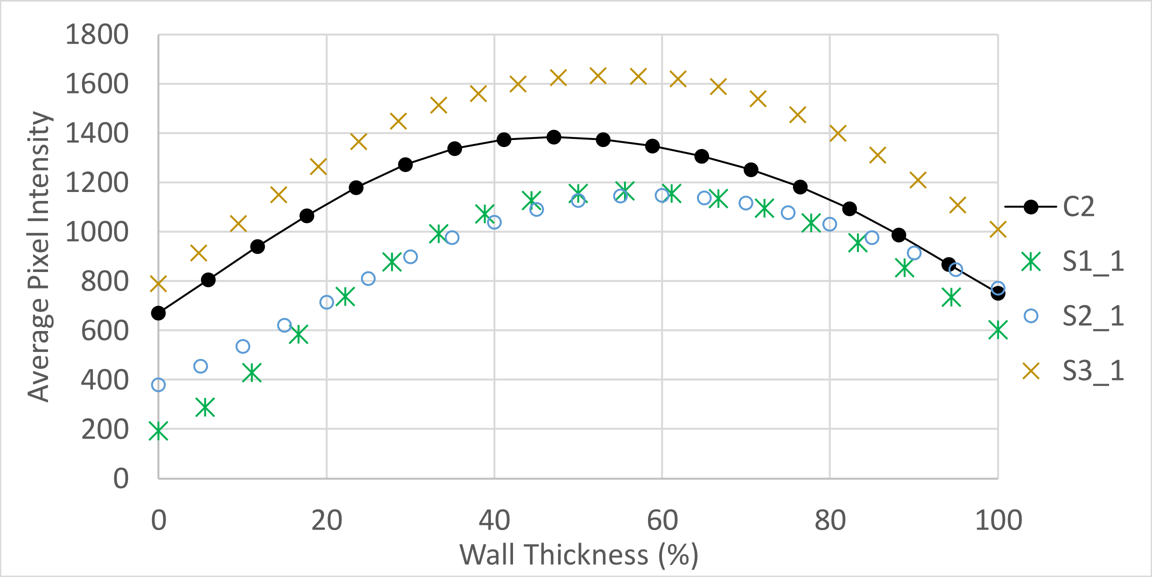

Figure 17. Average pixel intensity as a function of normalized wall thickness for samples from Animal 2.

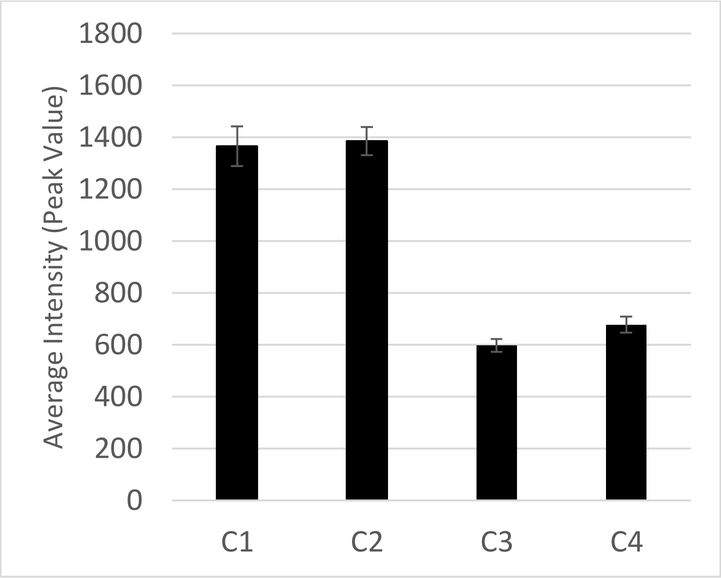

Figure 18. Peak values of average intensity for control samples. The values shown were used as the control values in determining the percent bright pixels. Error bars represent standard error for image averages (13 images minimum).

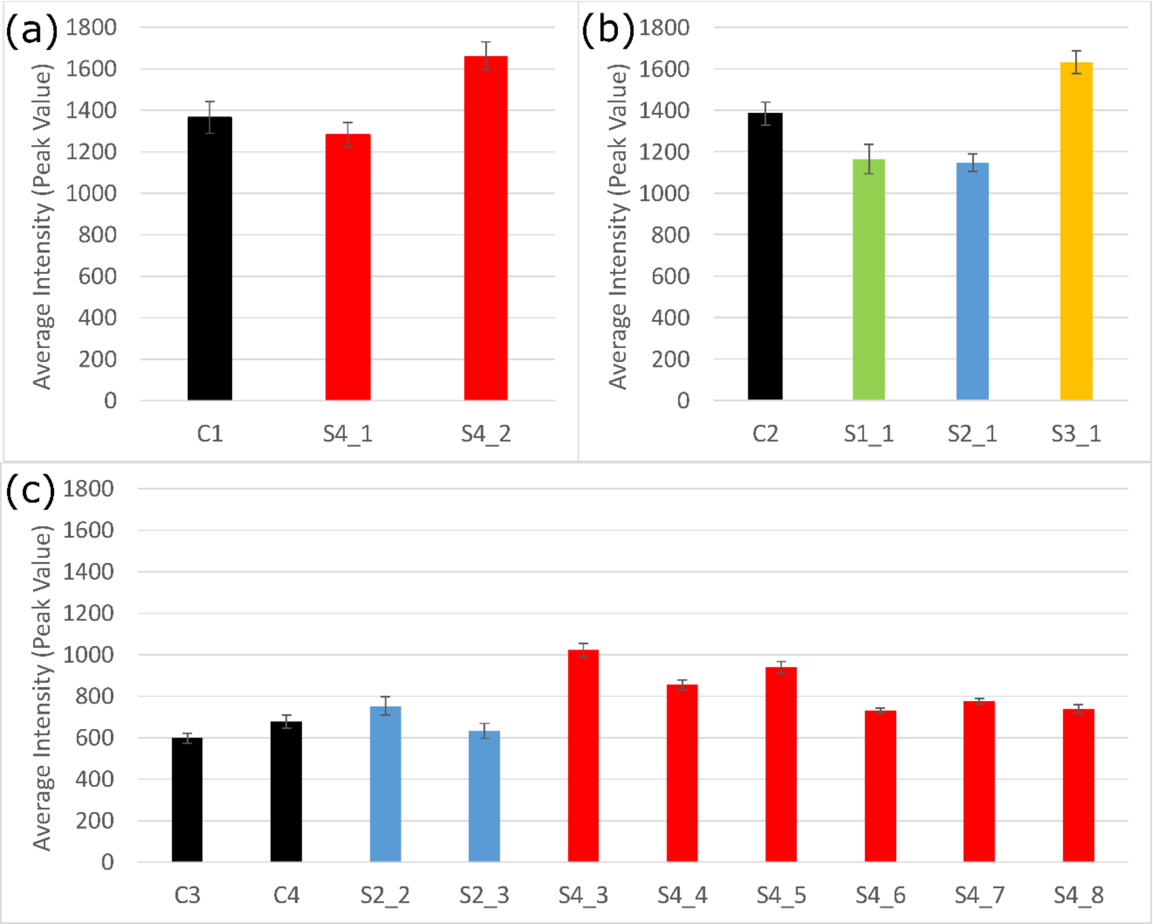

Figure 19. Peak values of average intensity for each sample. (a) samples from Animal 1. (b) samples from Animal 2. (c) samples from Animal 3. Error bars represent standard error for image averages (11 images minimum).

comparing samples from Animals 1 and 2 only (p = 0.7802) or from all animals (p = 0.94881). This was unsurprising, considering that there does not seem to be a significant difference in overall image brightness between the images from controls, and the images from damaged samples (see Figure 11, Figure 12, and Figure 13).

The maximum pixel intensity was also calculated for each confocal image of each sample, and plotted as a function of the normalized wall thickness; these graphs are shown in Figure 20. This metric was selected because it was hoped that it might detect the bright streaks in the confocal images. However, this metric shows little of interest, beyond the fact that for every sample except one, the maximum converges to the saturated value of 4095. Considering that even the images from Animal 3, which have lower average intensity values than those from Animals 1 and 2 (see Figure 19), converge to this value, it is likely that this convergence is a function of stray pixels or features such as dust or bubbles. ANOVA of values derived from averaging the peak brightness through the thickness showed no significant difference between control, subfailure, and failure groups ($p = .3280$). While this metric did not show anything of interest, it was included to show that it was explored. The maximum intensity, and Figure 20 will not be further referred to in the results.

The percentage of pixels having a brightness of more than double the control values (control values were 1375 for samples from the first or second ewe, 637 for samples from the third) is plotted as a function of normalized wall thickness in Figure 21. This metric was selected because it appeared that the high stretch level samples had very bright streaks, with much dimmer background pixels than corresponding controls. The metric clearly differentiates higher stretch level ($\lambda_{avg} = 1.6$ to failure) samples from both control and lower stretch level ($\lambda_{avg} = 1.3$ to 1.4). The peak values of all S3 ($\lambda_{avg} = 1.6$) and S4 (pulled to failure samples exceeded the peak values of all control, S1 ($\lambda_{avg} = 1.3$) and S2 ($\lambda_{avg} = 1.4$) samples. With the exception of S4_1, the peak values of all S3 and S4 samples were more than three times the highest peak value for an S2 sample (S2_2), with some of the S4 peak values as much as twenty times the peak value for

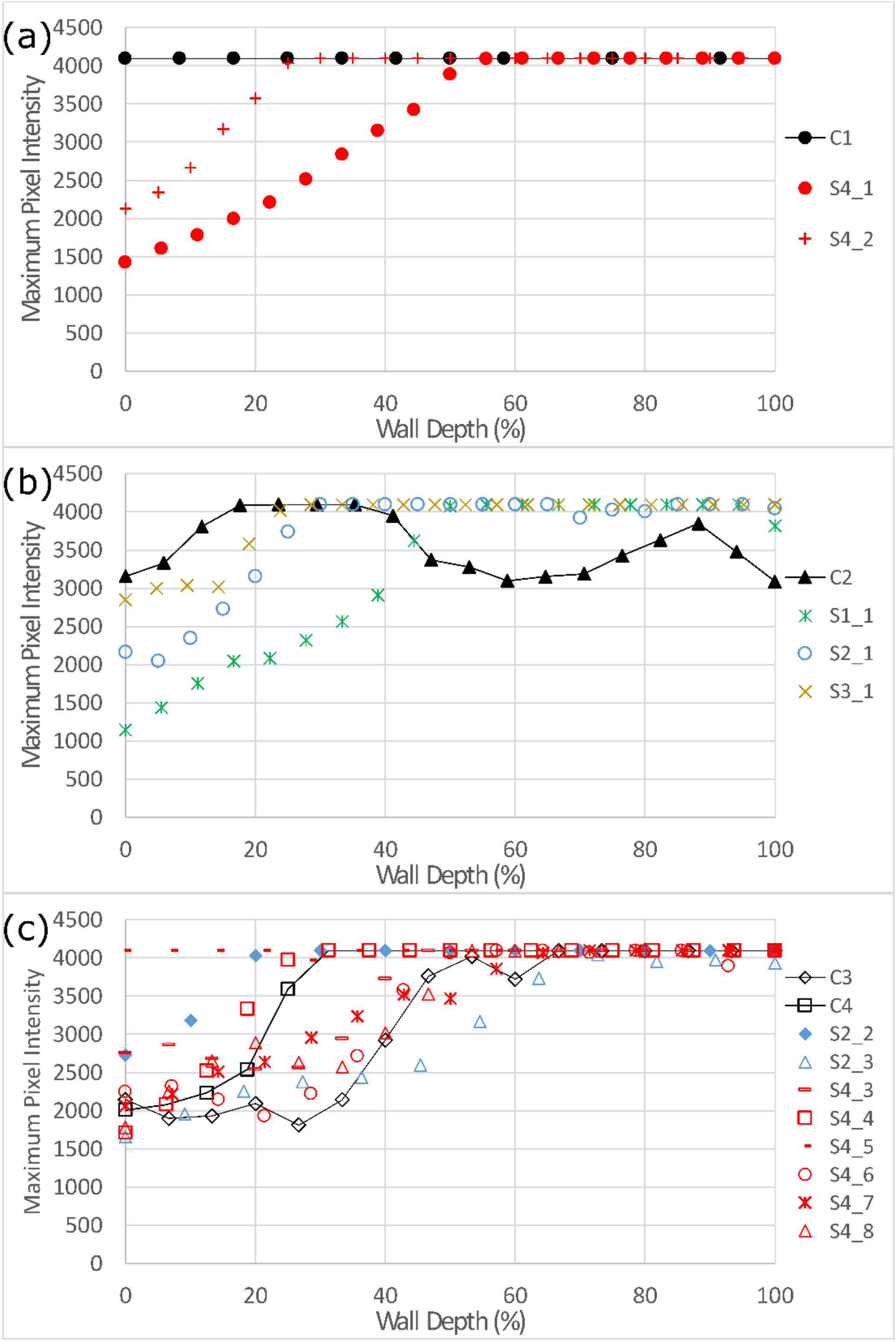

Figure 20. Maximum pixel intensity as a function of normalized wall depth. (a), (b) and (c) show samples from the first, second, and third animals, respectively. The saturated value (i.e., the maximum possible value for a pixel in these images) is 4095.

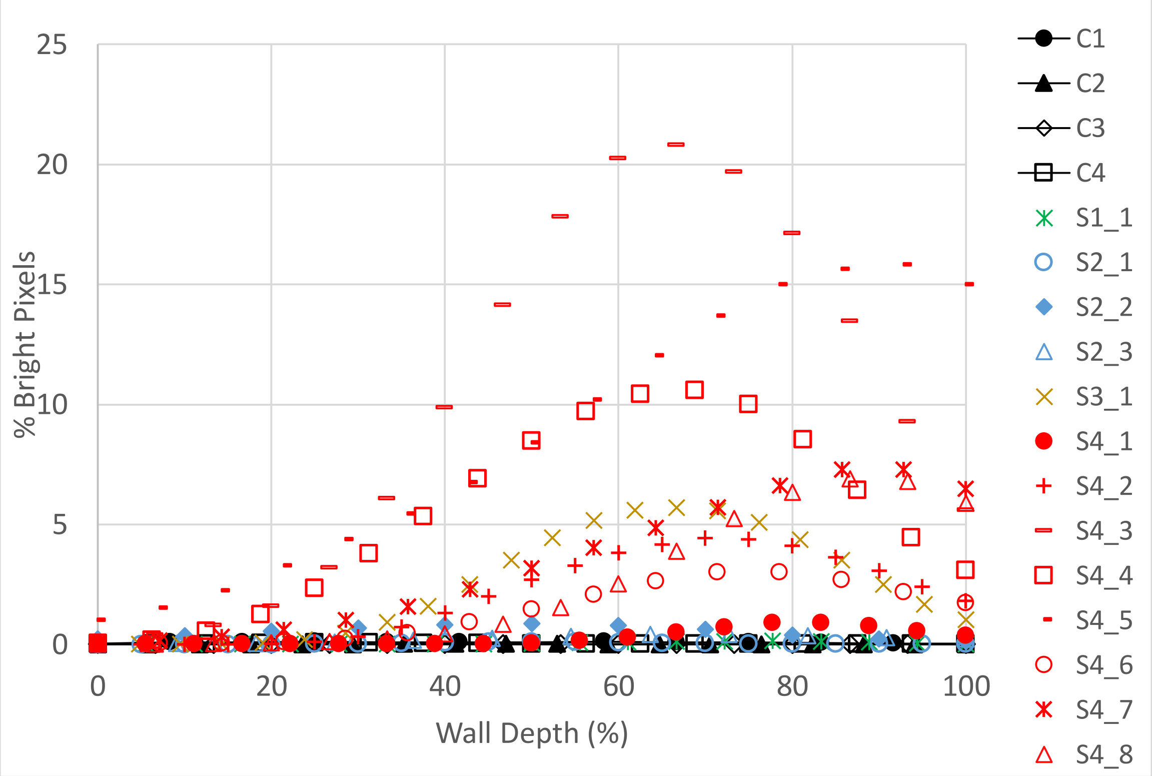

Figure 21. Percent bright pixels as a function of normalized wall depth. For simplicity, the points are color coded by stretch level (i.e., controls are in black, S1 in green, S2 in blue, S3 in brown, and S4 in red).

S2_2. While S4_1 does peak relatively low on the graph, its peak is still slightly above that of S2_2 (the S2 level sample with the highest peak in this graph), and well above the highest control value.

The same data are presented by animal in Figure 22. While samples from Animal 3 displayed a lower average brightness than those from Animals 1 and 2, some samples showed a much larger measure of percent bright pixels. A large degree of variation was

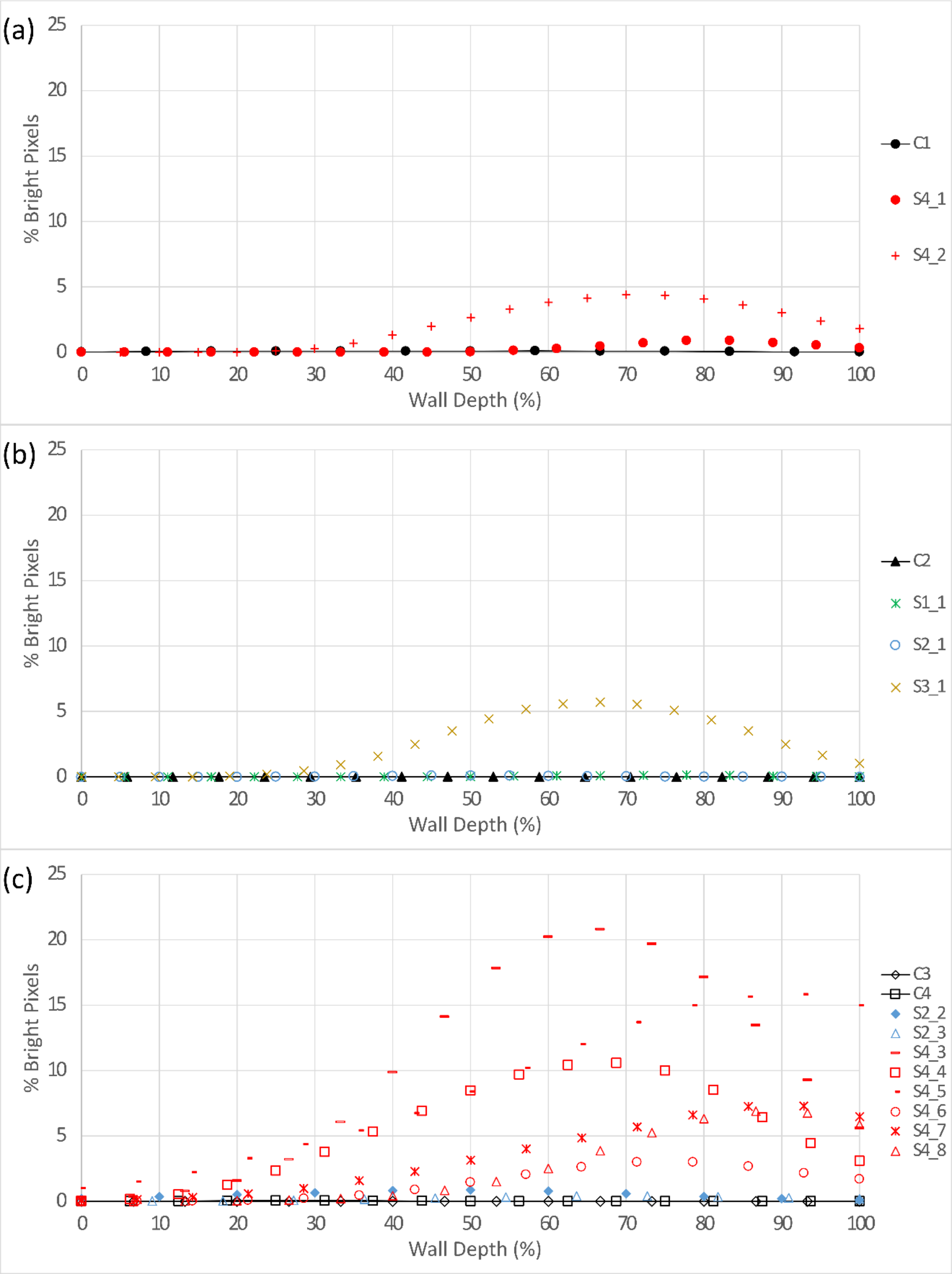

Figure 22. Percent bright pixels as a function of wall depth, by animal. (a) samples from Animal 1. (b) samples from Animal 2. (c) samples from Animal 3.

observed in this metric when comparing image sets taken from the same vessel segment (S4_6, S4_7, and S4_8, for instance), so that some of the difference between the animals may be accounted for in the natural variation across a vessel segment; that is to say, the locations imaged on the samples from Animals 1 and 2 may simply not have been the locations with the highest concentrations of CMP marking. S4_6, for instance, falls well within the same range as S4_2, whereas S4_7 and S4_8 (from the same vessel segment) have higher values. It is worth noting that the values of λ_{local} for S4_6, S4_7, and S4_8 (found by a measure over the entire imaging range of the vessel segment) as well as S4_2 were essentially identical (λ_{local} = 1.35). The extremely high values associated with the samples from Vessel 2 of Animal 3 (S4_3, S4_4, S4_5) may be due to higher values of local stretch (λ_{local} = 1.34-1.47) experienced by the vessel. It is clear from the confocal images (Figure 13), however, that these vessels do indeed show larger bright streaks compared to images from the first two animals.

The same data are replicated again in three forms in Figure 23, separated by stretch level. Examination of part (b), which shows S1 and S2 samples, reveals the possibility of a difference in peak percentages of bright pixels between S1 and S2 samples. It should be recalled, however, that S2_3 and S2_2 are separate image sets from the same blood vessel, so that more samples would be required to establish this conclusively.

Of note also in Figure 23 is the difference in the wall position at which the peak percentage of bright pixels occurs. While control, S1, and S2 samples often peak at or before 50 percent through the wall thickness, the S3 and S4 samples consistently peak

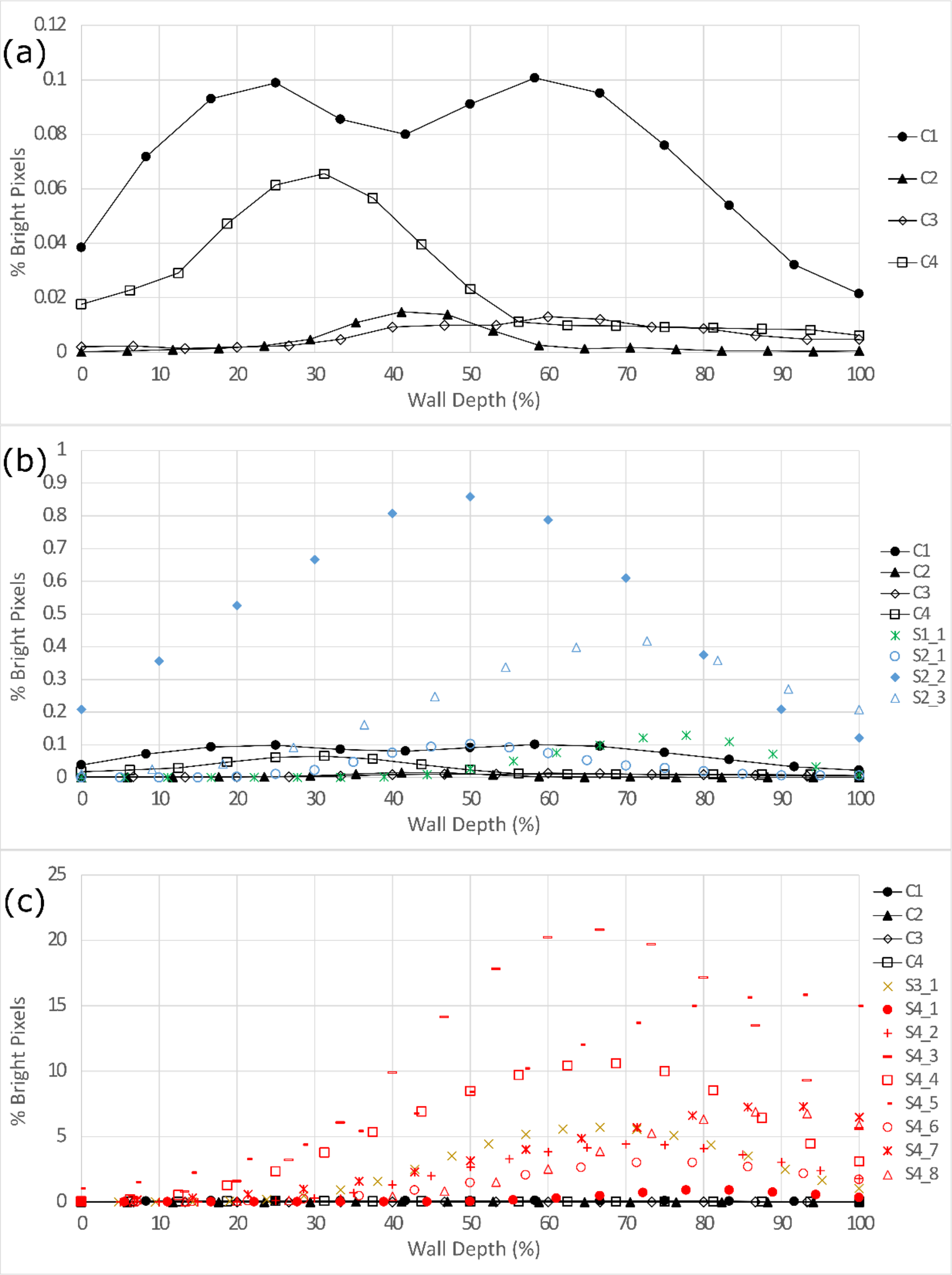

Figure 23. Percent bright pixels as a function of normalized wall depth. Data are the same as in Figure 21, but for visibility are grouped by stretch level. In order to better visualize the location at which peak values occur, it was necessary to present the graphs with different y-axes, so care should be taken in making comparisons between graphs. (a) presents the control sample data. (b) presents data from S1 and S2 samples. (c) presents data from S3 and S4 samples.

well above 50 percent through the thickness. While this observed difference could be due to the difficulty in defining the outside edge of the vessel in confocal images, especially the control images, which do not exhibit the unique bright streaks that clearly define the adventitial fibers in the S3 and S4 samples, it does agree with the observation that the collagen fibers to which CMP binds following high stretch events are primarily located in the adventitia or the outer media of the blood vessel wall.

The peak values of the percent bright pixel measurement are presented in Figure 24 as a function of the overstretch (λ_{local} in Table 1). In general, the data show an upward trend as stretch increases. The exception to this is S4_2, which exhibited a very high stretch level, but a relatively low percentage of bright pixels. This may be due in part to the fact that S4_2 was subject to several glitches in the control system during initial zero load length tests, exposing it to multiple high level stretches before the overstretch test. Even including this outlier, however, ANOVA comparison of the peak percent bright pixels showed a significant difference between control, subfailure, and failure groups ($p = 0.0035$). A t-test showed a significant difference between controls and failure level samples ($p = 0.0032$), and between subfailure and failure samples ($p = .0038$), but not between the control and subfailure samples ($p = 0.6536$). This agrees with observations made directly from the images, which showed a significant increase in the number of bright streaks between the samples with needle-to-needle stretch levels below 1.4, and those above this value, or pulled to failure.

The final metric was the number of peaks in the Hough transform per unit area, which is presented as a function of normalized wall thickness in Figure 25. This metric

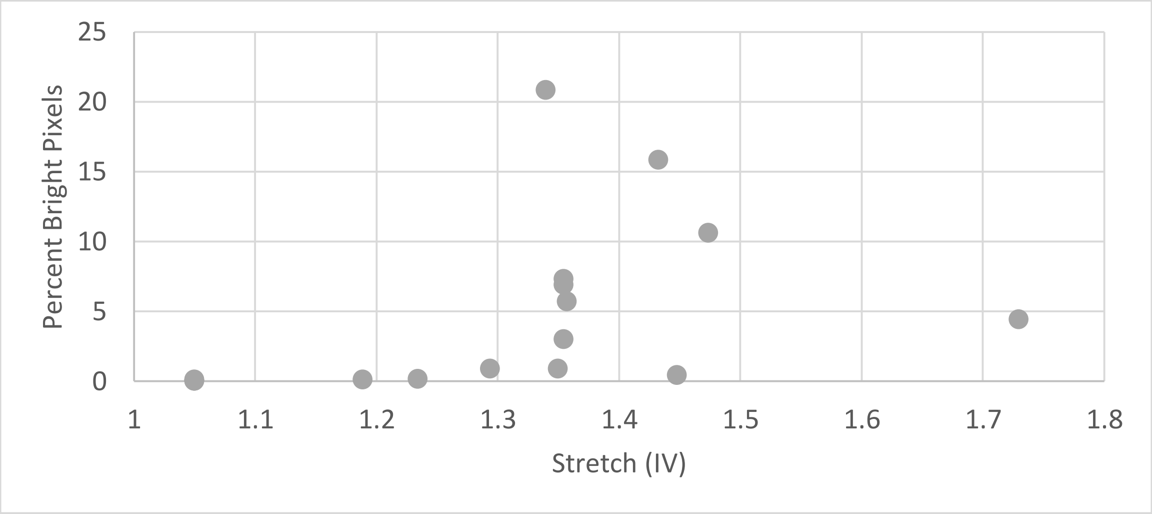

Figure 24. Peak percent bright pixels as a function of overstretch.

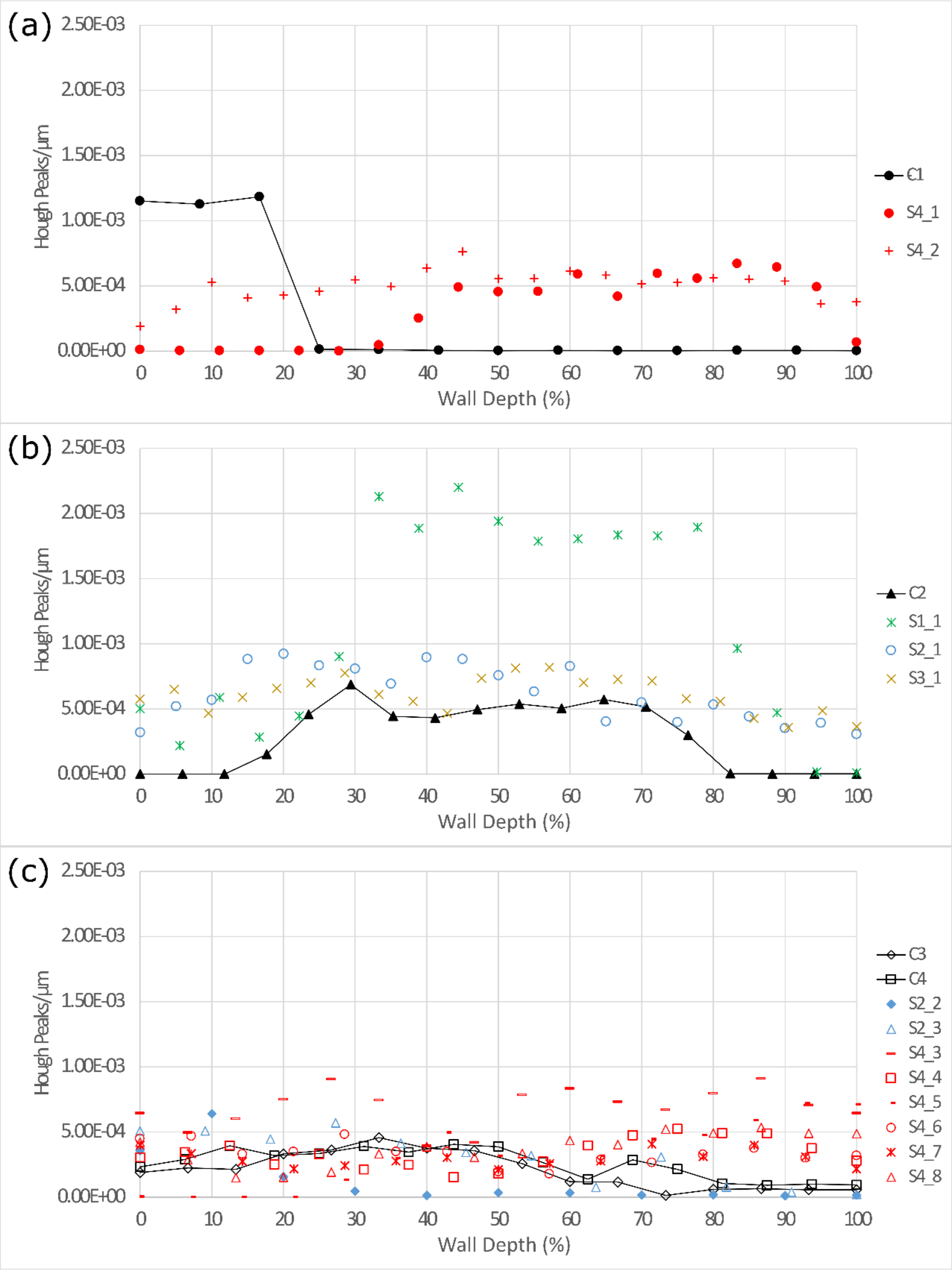

Figure 25. Hough lines per unit area. Samples from: (a) Animal 1; (b) Animal 2; (c) Animal 3.

was selected as it presented the possibility of counting the number of straight lines in the images, perhaps allowing a “number of streaks” metric. The graphs are presented by animal, so that (a) shows samples from Animal 1, (b) from Animal 2, and (c) from Animal 3. While S4 samples from Animal 1 and Animal 3 showed higher values of this metric in the adventitia than their respective controls, samples from Animal 2 do not appear to show a correlation between the maximum overstretch, and the values of this metric. Average values of this metric through thickness are shown in Figure 26. ANOVA of these values showed no statistical difference between control, subfailure, and failure groups ($p = 0.1558$).

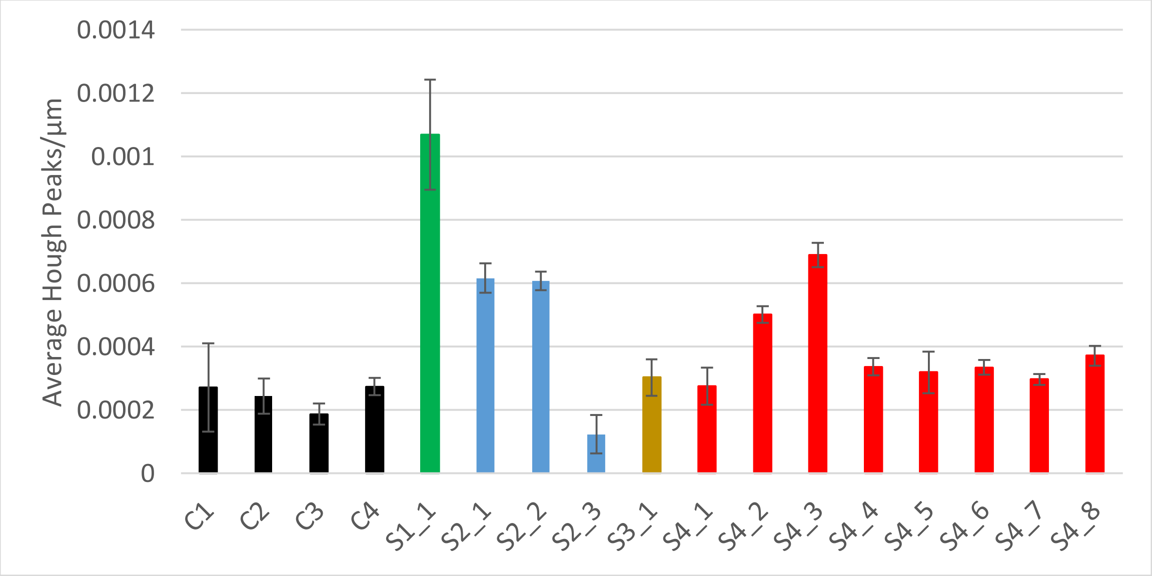

Figure 26. Average number of Hough peaks per µm. Error bars denote standard error.

CHAPTER 4

DISCUSSION

The purpose of this study was to investigate and characterize the effectiveness of CMP as a marker for damage to cerebral blood vessels subjected to various levels of axial overstretch. Investigation of incubation time showed that while similar features are visible as a result of 1-hour and overnight incubation times, the background appears to be brighter as compared to features of interest in the 1-hour samples. Qualitative evaluation of fluorescence and confocal microscopy images showed bright streaks in images subjected to high levels of axial stretch. Confocal stacks revealed that these bright streaks were primarily concentrated in the outer parts of the vessel wall, suggesting that fibrous, axially oriented structures in the adventitia were the primary locations of damage to collagen. Quantification of images from the confocal stacks revealed no significant difference in the average brightness of the brightest image between controls and damaged samples. The percentage of image pixels with brightness above a threshold proved a valuable metric for differentiating samples pulled to failure from controls, but not for differentiating between controls and samples pulled to subfailure levels.

Location of Damaged Collagen Fibers

It is suggested that the bright, axially oriented structures visible in fluorescence and confocal images of damaged samples represent CMP binding to denatured collagen in fibrous, axially oriented structures of the adventitia, which are damaged during axial overstretch. This hypothesis is based in two factors: 1) the fact that confocal images show these features primarily in the outer part of the blood vessel, and 2) previous work has shown a significant portion of the adventitia in cerebral vessels to be composed of axially oriented collagen fibers (Finlay et al., 1995; Wicker et al., 2008).

Direct observation of the confocal images in Figure 11, Figure 12, and Figure 13 clearly shows the appearance of the bright streaks to be best visible in the adventitia images. Examination of images from the same vessel segment, such as S4_6, S4_7, and S4_8 in Figure 13, shows that these features continue along the length of the vessel in a similar location circumferentially. While the location of the peak value of the percent bright pixels was not analyzed statistically, it was observed that the peak of this metric generally appeared to occur beyond 50 percent of the way through the wall thickness in samples which were pulled to failure.

An understanding of the previous work done in characterizing the structure of cerebral vessels is important to interpreting the images from this study, since confocal images from the media of damaged samples show bright, streak like features, similar to those in the adventitia images (Figure 11, Figure 12, and Figure 13). While it may be tempting to interpret these streaks as damage to collagen fibers in the media, previous work in cerebral arteries suggests that medial collagen is nearly circumferentially oriented, whereas collagen fibers in the adventitia tend to be more axially oriented (Finlay et al., 1995; Wicker et al., 2008). As such, it is far more likely that the appearance of these features in images of the media is due to the low z-resolution of the confocal setup used. Either a higher magnification interrogation of these samples, or a more sophisticated setup with higher z-resolution at the same magnification, could serve to better establish the location of these features.

Quantification of CMP

Damage Marking

Four metrics for quantifying damage marked by CMP staining were proposed in the Methods section of this study: maximum pixel intensity, average pixel intensity, percent bright pixels, and number of lines, as counted by the Hough transform. Of these four, only one, the percent bright pixels, was found to show a statistical difference between control samples, and damaged ones.

Even the percent bright pixels, however, failed to show a statistically significant difference between controls, and samples pulled to subfailure stretch levels. It is possible that the failure to demonstrate a significant difference between controls and subfailure samples was due to the small number of subfailure samples (one or two vessel segments per stretch level) used. A larger number of subfailure stretch samples may serve to better show a significant difference between subfailure stretch levels (especially stretch levels in the vicinity of those experienced by S3_1, i.e., $\lambda_{local} > 1.4$), and controls; however, the abrupt change in staining between the samples exposed to the lower stretch levels (λ_{avg} = 1.3-1.4) and the samples exposed to high or failure level overstretch (λ_{avg} = 1.6 to failure) suggests that the difference between controls and subfailure samples is more subtle, and may require a more sophisticated metric.

Average brightness failed to show a difference between controls and damaged samples. This may be due in part to the large brightness difference between samples from Animals 1 and 2, and from Animal 3, resulting in the requirement to either break up samples by animal, resulting in small groups, or to use groups with an artificially high degree of variation; thus, further investigation of this metric may be warranted. In the current study, however, the average brightness did demonstrate that in general, the brightest images of the sample were obtained from the center of the wall. It is likely that this is due to the amount of surrounding tissue, and the low z-resolution of the confocal imaging method used. In the center of the tissue, there is a maximal amount of tissue within the optical slice obtained by the microscope, so that images have brighter background values; as such, this metric may serve as a useful means of determining the location in the vessel wall in future studies, removing some of the subjectivity in the process of selecting the inner and outer edges of the vessel. The medial location of the peak value of average brightness lends greater strength to the results of the percent bright pixel quantification. While the average brightness generally peaked in the media of the vessel, the percent bright pixels generally appeared to peak in the adventitia of vessels exposed to failure level overstretches.

While the statistical analysis of some metrics may have been improved by a larger sample size, the sample size used in this study was sufficient to show a statistically significant difference in CMP staining of cerebral blood vessels between control samples, and samples pulled axially to failure. While more subfailure samples may be advisable in future studies, the focus on failure level samples in this study was essential to this initial quantification.

IEL Failure Compared to CMP Marking

Comparison of IEL failure observations and CMP marking observations is advisable for two reasons. Firstly, previous work in noncerebral arteries (Fonck et al., 2007; Wan et al., 2010) has suggested an interaction between elastin and collagen structures in mechanical loading of blood vessels. Given that during mechanical testing of the vessels used in this study, IEL failure was generally observed at close to the same stretch levels at which CMP staining became most pronounced, it is advisable that this interaction be addressed. Secondly, while CMP presents a relatively easy method of staining for damage due to high levels of axial stretch, observation of IEL failure requires no staining whatsoever, as the IEL is present as a part of vessel microstructure. Thus, close examination of the IEL for layer failure may present an alternative to the use of CMP staining in identifying damaged regions.

Large-scale IEL failure, as mentioned previously, was visible in all samples stretched to failure (S4). It is of great interest that this is also the level of stretch associated with the most CMP staining. Previous work in other blood vessels has suggested that loss of functional elastin structures causes a significant change in mechanical response of blood vessels, whether the vessel has been allowed to remodel to adapt to this condition (Wan et al., 2010), or not (Fonck et al., 2007). Thus, it is possible that extensive damage to the IEL and other elastin structures could result in changes to the response of load bearing collagen fibers in the adventitia. Given that collagen is both much stiffer and much stronger than elastin (Finlay et al., 1998); however, it seems unlikely that the elastin structures would carry a significant enough portion of the load to cause IEL failure prior to failure of collagen structures. It is posited as a more likely theory that local damage to load bearing collagen structures results in high levels of local stretch as the load is taken up by other fibers. This high level of local stretch would result in failure of the IEL.

This hypothesis is supported by images of S3_1, which exhibited no visible layer failure of the IEL, but shows staining comparable with S4 samples, as demonstrated by direct observation of fluorescence (Figure 10) and confocal images (Figure 13), and by the percent bright pixels metric (Figure 21). S3_1 was unique in that it was subjected to multiple overstretches of increasing severity in an attempt to achieve the highest possible subfailure overstretch. Previous work in cerebral arteries (Bell et al., 2015) has shown that subfailure overstretch results in permanent changes to the mechanical properties of a vessel, possibly due to rearrangement of the microstructure. If such rearrangement of the microstructure caused more even load distribution across collagen structures in the adventitia, it is possible that a level of damage sufficient to cause CMP binding to collagen structures might occur without the high local stretch phenomena associated with IEL failure.

While one instance of IEL layer failure was visible in S2_2, this failure occurred very near the end of mechanical testing (3 frames prior to the maximum overstretch), whereas the first occurrence of IEL failure visible in failure level samples was generally earlier in the overstretch process. Also, in most cases, failure level samples exhibited many instances of IEL failure, compared to the single instance exhibited by S2_2. The fact that a single instance of IEL failure in S2_2 was insufficient to cause CMP binding comparable with that observed in S4 samples suggests that failure of multiple large collagen structures is necessary to obtain widespread CMP binding. More work is required in order to establish the relationship between CMP binding and IEL layer failure during axial overstretch.

IEL failure may be a useful method of detecting mechanical damage due to axial overstretch under the correct conditions. As a marker for damage, however, CMP presents the advantage of being readily visible in fluorescence images with relatively low magnification, reducing the effort required in order to identify damage locations. Also, considering it is likely that most axial loading is carried by the collagen structures in the blood vessel, CMP presents the advantage of marking the structures which are actually damaged. While this study did not attempt higher magnification interrogation of the samples, it is probable that such interrogation would provide a better understanding of what structures are damaged during overstretch.

Potential for Use In Vivo

The methods used in this study show promise for in vivo, or at least in situ application. A confocal approach similar to that used in this study could be used for imaging intact vessels, at least on the surface of the brain. An excellent first step toward implementing this method would be to repeat this study, but image vessels in an intact state, rather than cutting them open and laying them flat on the slide. In order for this study to best succeed, it would be advisable to use a different confocal setup, or a higher magnification in order to obtain stacks with better z-resolution.

CMP could be administered via the bloodstream by perfusion for later in situ imaging, or by injection into a living animal shortly after injury. If this administration method proved a problem, the CMP could also be administered to surface vessels simply by soaking the intact brain tissue in CMP; using the soaking method might also eliminate the need to re-evaluate concentration or incubation time as factors in the staining process.

Initial forays into in situ staining and imaging done in parallel with this study proved challenging. Little was understood about the nature of the features that CMP staining would present, and initial experiments were carried out using brain tissue from mice, with much smaller vessels than those used in this study. Where possible, the use of tissue similar to that used in this study (i.e., large cerebral vessels from lambs) may provide a better starting point for evaluation of CMP as a marker of damage in situ.

Effects of Incubation Time

This study qualitatively compared images from samples with 1-hour and overnight incubation times. A significant difference in overall image brightness was noted. This is likely due to the amount of CMP binding which has occurred at the time point in question. When brightened, the images incubated for 1-hour showed similar features to those from the 18-hour incubation; however, the difference between background pixels and the bright streaks observed in damaged samples was much smaller in the samples from the 1-hour incubation time. This suggests that while CMP binding has begun at the 1-hour time point, a large portion of the background staining also occurs during this time. By the 18-hour time point, background staining has likely slowed, while staining of damaged features has not. For this reason-i.e., the increased difference between background pixels and features of interest, the 18-hour incubation period is suggested. The 18-hour incubation period is also advantageous in that the processes of removing the lamb brain, dissecting vessels, and testing them often result in the staining incubation time beginning around the normal end of the workday. The overnight incubation period allows for a researcher to maintain normal working hours, while simultaneously obtaining improved results.

Confocal Image Selection

The process used in selecting the locations from which to obtain confocal images for damage evaluation and quantification necessarily involved some human interpretation. In most cases, avoiding the failed edge and the suture region resulted in a relatively constrained space within which to image, so that little risk of human influence in the procedure existed. Where a risk of human influence on the selection of imaging sites did exist, it was primarily focused on minimizing the number of branches in the region of interest. In the case of vessels from Animal 3, virtually the entire vessel area, with the exception of areas within a field of view of failed edges or suture locations, was imaged and analyzed. While a broad level of variation of the percent bright pixels did exist in images from different regions of the same vessel, the regional variation was much smaller than the variation between failure and subfailure samples.

The exclusion of the suture region was deemed necessary, since it was subject to end effects associated with the constraint imposed by the suture. In general, the suture region showed IEL failure (although this failure appeared most often as jagged, joined tears, rather than the relatively straight, single line observed in the layer failures seen during mechanical testing), and bright streaks of CMP staining.

The decision to avoid failed edges almost certainly reduced the level of CMP staining observed in samples pulled to failure, since the failed edges were stained very brightly. It was decided early in the study, however, that a greater interest should be placed on regions not subject to failure, since the usefulness of a marker for failed blood vessels is relatively limited.

Differences in Brightness Between Animals

While little difference in average brightness existed between samples from Animals 1 and 2, samples from Animal 3 were shown to be significantly less bright. It is possible that this brightness difference is due to a number of factors associated with variations between animals (i.e., vessel wall thickness, collagen content). While the vessel walls were generally found to be thinner in this animal than in the previous two, these measurements were made by confocal imaging, so that a change in staining could have affected the measurements. It is possible that minor variations in the staining procedure, such as a small difference in concentration or the heating time of the CF-CMP solution could be responsible for these differences, and may have resulted in the differences in measured wall thickness.

Outliers

Examination of Table 1 will immediately reveal that S4_2 experienced a very high overstretch, inconsistent with the stretch levels experienced by other S4 vessels. This very high level of overstretch, combined with a relatively low percent of bright pixels in its adventitial images, causes it to sit far outside the general trend shown in Figure 24 (with this value, an exponential fit by Excel of the data shown in Figure 24 gives R^2 = .6014; removing the point gives R^2 = .7298). The extremely high stretch value experienced by this vessel is partially explained by the fact that the vessel experienced multiple unintentional overstretches due to program error during its zero load tests. These extra overstretches prior to pulling the vessel to failure would act to change the mechanical properties of the vessel (Bell et al., 2015). It is worth mentioning that S3_1 may have experienced a similar effect, since it was exposed to multiple overstretch tests in order to achieve a higher subfailure overstretch.

CHAPTER 5

CONCLUSIONS

This study has demonstrated the promise of CMP as a marker for collagen damage caused by mechanical injury. The percent of pixels in an image that fell above the threshold value (determined using a control sample from the same animal) proved an effective method of quantifying damage for isolated vessel studies such as this one. It is suggested that this metric be used in future studies.

The results of this study suggest that axially oriented mechanical overstretch of cerebral blood vessels causes damage to fibrous, axially oriented collagen structures in the adventitia. It was observed that some connection exists between damage to these adventitial structures and layer failure of the IEL, implying that axial overstretch injuries to blood vessels due to TBI could lead to later issues related to IEL damage, such as aneurysm (Mizutani et al., 2001; Yamazoe et al., 1990).

Limitations and Future Work

While the percent bright pixels was shown to follow a generally upward trend as local stretch level increased, care should be taken in using any correlation with either of the stretch measures provided in this study outside of the context of an axial stretch test. The needle-to-needle measurement used in calculating λ_{avg} presents the advantage of being straightforward to calculate from test data; however, due to the constraints imposed by mounting the vessel segments on needles, end effects do exist near the needles, so that needle-to-needle stretch is generally higher than the actual stretch values experienced by most of the vessel. Microsphere measurements are also problematic in that the microspheres are loosely caught in the fibers of the adventitia, presenting some uncertainty about whether the motion of microspheres is actually the same as the motion of the vessel wall. Further, in many cases, microsphere measurements can be inflated or deflated as events such as IEL layer failure occur during testing, causing microspheres to move rapidly, and sometimes leave the vessel entirely. Future work involving a more reliable measure of stretch will be invaluable to in vivo application of CMP staining.

While percent bright pixels presents a promising metric for quantifying the level of overstretch to which a vessel was exposed, some limitations to the method do exist. Examination of the average brightness metric showed that it followed a bell curve or parabolic shape through the thickness of the vessel, so that images close to the inner and outer edges of the vessel wall had a much lower average brightness than those in the center. As only the peak value of the control curves was used in determining the percent bright pixels, it is probable that the method used in this study provides an underestimate in images far from the center of the stack. Since the peak value of the percent bright pixels generally did not occur at the center of the vessel wall in the damaged vessels, it is possible that use of control values by wall depth could drastically improve the sensitivity and/or consistency of this metric.

A more serious limitation to this method is the need for a control value in order to compare vessels across animals. While a control value is available in isolated vessel studies such as this one, no such value may be available in studies where vessels are imaged in vivo or in situ after an animal has been exposed to a head injury. Thus, while percent bright pixels is a valuable metric in initial studies such as this one, and may continue to be a valuable metric for comparing vessel injuries within a single animal, comparison across animals may require a more sophisticated metric for in vivo or in situ models.

Implementation of the Hough transform code prepackaged with Matlab proved more difficult than anticipated. The code did not account for line orientation, and mapping lines back to the original images for validation proved too time consuming to attempt. Recent work has shown the usefulness of OrientationJ in providing orientation data for collagen fibers in blood vessels (Rezakhaniha et al., 2012). It is likely that use of this code on the images from this study would prove more effective than attempting to custom write code.

While this study observed some relationship between IEL layer failure and CMP staining, no formal attempt at determining correlation or causation relationships between the two was made. Understanding of how IEL failure is related to overstretch events could have significant bearing on the relationship observed between TBI and secondary conditions such as stroke (Burke et al., 2013; Chen et al., 2011), especially considering that IEL damage has long been considered to play a role in the development of aneurysms (Mizutani et al., 2001; Yamazoe et al., 1990). Further work should include more detailed interrogation of the interaction between IEL failure and collagen damage. This could be as simple as high magnification confocal stacks of tears in the IEL from samples similar to those of this study.

APPENDIX

Matlab Code

Masking Script: Demo.m

```matlab
% Demo of how masking procedure was performed
clear; clc; close all

% Stack together 'n' adjacent z-stack from left to right
Istack = StackNStitch;
%%
% Mask this combined z-stack
[Imasked, Mask] = CreateMask(Istack);

% Enter vessel label for saving
name = inputdlg('Enter Vessel Label'); % such as "M4_1"
name = name{1};

% Save masked Image with label
eval([name,'_masked = Imasked;']);
eval(['save ',name,'_masked.mat ',name,'_masked']);

% Save mask with label
eval(['Mask_',name,' = Mask;']);
eval(['save ','Mask_',name,'.mat Mask_',name]);
%%
%Save original stack:
[rows cols slices] = size(Istack);

eval(['mkdir ',name]);
eval(['cd ',name]);

for sliceNum = 1:slices

    currentSlice = Istack(:,:,sliceNum);
    if(sliceNum <2)
        imwrite(currentSlice,[name,'.tif']);
    else
        imwrite(currentSlice,[name,'.tif'],'WriteMode','append');
    end


end
```

```
cd ..
```

Stack Analysis Script for Analyzing Metrics: stackScriptNew.m

```
%%%%%%%%%%%%%%%%%%%%%%%%%%%%%%%%%%%%%%%%%%%%%%%%%%%%%%%%%%%%%%%%%%%%%%%
%%%%
%%% stackScriptNew runs stackAnalysis_ctrl to find metrics about each
vessel
%%% sample based upon its associated control.
%%%
%%%%%%%%%%%%%%%%%%%%%%%%%%%%%%%%%%%%%%%%%%%%%%%%%%%%%%%%%%%%%%%%%%%%%%%
%%%%
clear; clc; close all;

ctrlBrightness_bright = 1375;
ctrlBrightness_dim = 637;

%%%%%%%%%%%%%%%%%%%%%%%%%%%%%%"Bright"
group:%%%%%%%%%%%%%%%%%%%%%%%%%%%%%

C1FileName = 'C1_masked.mat';
C2FileName = 'C2_masked.mat';

M1_1FileName = 'M1_1_masked.mat';

M2_1FileName = 'M2_1_masked.mat';

M3_1FileName = 'M3_1_masked.mat';

M4_1FileName = 'M4_1_masked.mat';
M4_2FileName = 'M4_2_masked.mat';

%%%%%%%%%%%%%%%%%%%%%%%%%%%%%% Perform Stack analysis
%%%%%%%%%%%%%%%%%%%%

%C1
[C1AvgB, C1PkB,C1HotPix C1Pcts C1PeaksNorm, C1MStack,C1HStack]...
    = stackAnalysis_ctrl(C1FileName,ctrlBrightness_bright);
%C2
[C2AvgB, C2PkB,C2HotPix C2Pcts C2PeaksNorm, C2MStack, C2HStack]...
    = stackAnalysis_ctrl(C2FileName,ctrlBrightness_bright);

%M1_1
[M1_1AvgB, M1_1PkB,M1_1HotPix M1_1Pcts M1_1PeaksNorm,
M1_1MStack,M1_1HStack]...
    = stackAnalysis_ctrl(M1_1FileName,ctrlBrightness_bright);

%M2_1
[M2_1AvgB, M2_1PkB,M2_1HotPix M2_1Pcts M2_1PeaksNorm,
M2_1MStack,M2_1HStack]...
```

```
    = stackAnalysis_ctrl(M2_1FileName,ctrlBrightness_bright);

%M3_1
[M3_1AvgB, M3_1PkB,M3_1HotPix M3_1Pcts M3_1PeaksNorm, M3_1MStack,
M3_1HStack]...
    = stackAnalysis_ctrl(M3_1FileName,ctrlBrightness_bright);

%M4_1
[M4_1AvgB, M4_1PkB,M4_1HotPix M4_1Pcts M4_1PeaksNorm, M4_1MStack,
M4_1HStack]...
    = stackAnalysis_ctrl(M4_1FileName,ctrlBrightness_bright);
%M4_2
[M4_2AvgB, M4_2PkB,M4_2HotPix M4_2Pcts M4_2PeaksNorm, M4_2MStack,
M4_2HStack]...
    = stackAnalysis_ctrl(M4_2FileName,ctrlBrightness_bright);


%%%%%%%%%%%%%%%%%%%%%%%%%%%%%%"Dim"
group:%%%%%%%%%%%%%%%%%%%%%%%%%%%%%%%%%

C3FileName = 'C3_masked.mat';
C4FileName = 'C4_masked.mat';

M2_2FileName = 'M2_2_masked.mat';
M2_3FileName = 'M2_3_masked.mat';

M4_3FileName = 'M4_3_masked.mat';
M4_4FileName = 'M4_4_masked.mat';
M4_5FileName = 'M4_5_masked.mat';
M4_6FileName = 'M4_6_masked.mat';
M4_7FileName = 'M4_7_masked.mat';
M4_8FileName = 'M4_8_masked.mat';

%%%%%%%%%%%%%%%%%%%%%%%%%%%%%% Perform Stack analysis
%%%%%%%%%%%%%%%%%%%%

%C3
[C3AvgB, C3PkB,C3HotPix C3Pcts C3PeaksNorm, C3MStack, C3HStack]...
    = stackAnalysis_ctrl(C3FileName,ctrlBrightness_dim);
%C4
[C4AvgB, C4PkB,C4HotPix C4Pcts C4PeaksNorm, C4MStack, C4HStack]...
    = stackAnalysis_ctrl(C4FileName,ctrlBrightness_dim);

%M2_2
[M2_2AvgB, M2_2PkB,M2_2HotPix M2_2Pcts M2_2PeaksNorm,
M2_2MStack,M2_2HStack]...
    = stackAnalysis_ctrl(M2_2FileName,ctrlBrightness_dim);
%M2_3
[M2_3AvgB, M2_3PkB,M2_3HotPix M2_3Pcts M2_3PeaksNorm, M2_3MStack,
M2_3HStack]...
    = stackAnalysis_ctrl(M2_3FileName,ctrlBrightness_dim);

%M4_3
[M4_3AvgB, M4_3PkB,M4_3HotPix M4_3Pcts M4_3PeaksNorm, M4_3MStack,
M4_3HStack]...
```

```
    = stackAnalysis_ctrl(M4_3FileName,ctrlBrightness_dim);
%M4_4
[M4_4AvgB, M4_4PkB,M4_4HotPix M4_4Pcts M4_4PeaksNorm, M4_4MStack,
M4_4HStack]...
    = stackAnalysis_ctrl(M4_4FileName,ctrlBrightness_dim);
%M4_5
[M4_5AvgB, M4_5PkB,M4_5HotPix M4_5Pcts M4_5PeaksNorm, M4_5MStack,
M4_5HStack]...
    = stackAnalysis_ctrl(M4_5FileName,ctrlBrightness_dim);
%M4_6
[M4_6AvgB, M4_6PkB,M4_6HotPix M4_6Pcts M4_6PeaksNorm, M4_6MStack,
M4_6HStack]...
    = stackAnalysis_ctrl(M4_6FileName,ctrlBrightness_dim);
%M4_7
[M4_7AvgB, M4_7PkB,M4_7HotPix M4_7Pcts M4_7PeaksNorm, M4_7MStack,
M4_7HStack]...
    = stackAnalysis_ctrl(M4_7FileName,ctrlBrightness_dim);
%M4_8
[M4_8AvgB, M4_8PkB,M4_8HotPix M4_8Pcts M4_8PeaksNorm, M4_8MStack,
M4_8HStack]...
    = stackAnalysis_ctrl(M4_8FileName,ctrlBrightness_dim);



%%
%%%%%%%%%%%%%%%%%%%%%%%%%%%%%%%%Plots%%%%%%%%%%%%%%%%%%%%%%%%%%%
%%%%

%BrightPixels:
figure(1);
clf;
hold on;

plot(C1Pcts,C1HotPix,'-ok');
plot(C2Pcts,C2HotPix,'-dk');
plot(C3Pcts,C3HotPix,'-sk');
plot(C4Pcts,C4HotPix,'-^k');
plot(M1_1Pcts,M1_1HotPix,'-oc');
plot(M2_1Pcts,M2_1HotPix,'-or');
plot(M2_2Pcts,M2_2HotPix,'-dr');
plot(M2_3Pcts,M2_3HotPix,'-sr');
plot(M3_1Pcts,M3_1HotPix,'-og');
plot(M4_1Pcts,M4_1HotPix,'-ob');
plot(M4_2Pcts,M4_2HotPix,'-db');
plot(M4_3Pcts,M4_3HotPix,'-sb');
plot(M4_4Pcts,M4_4HotPix,'-^b');
plot(M4_5Pcts,M4_5HotPix,'-*b');
plot(M4_6Pcts,M4_6HotPix,'-xb');
plot(M4_7Pcts,M4_7HotPix,'-pb');
plot(M4_8Pcts,M4_8HotPix,'-hb');
legend('C1','C2','C3','C4','M1_1','M2_1','M2_2','M2_3','M3_1','M4_1','M
4_2','M4_3','M4_4','M4_5','M4_6','M4_7','M4_8');

[maxBP(1,1) maxBPI(1,1)] = max(C1HotPix);
[maxBP(2,1) maxBPI(2,1)] = max(C2HotPix);
[maxBP(3,1) maxBPI(3,1)] = max(C3HotPix);
[maxBP(4,1) maxBPI(4,1)] = max(C4HotPix);
```

```
[maxBP(5,1) maxBPI(5,1)] = max(M1_1HotPix);
[maxBP(6,1) maxBPI(6,1)] = max(M2_1HotPix);
[maxBP(7,1) maxBPI(7,1)] = max(M2_2HotPix);
[maxBP(8,1) maxBPI(8,1)] = max(M2_3HotPix);
[maxBP(9,1) maxBPI(9,1)] = max(M3_1HotPix);
[maxBP(10,1) maxBPI(10,1)] = max(M4_1HotPix);
[maxBP(11,1) maxBPI(11,1)] = max(M4_2HotPix);
[maxBP(12,1) maxBPI(12,1)] = max(M4_3HotPix);
[maxBP(13,1) maxBPI(13,1)] = max(M4_4HotPix);
[maxBP(14,1) maxBPI(14,1)] = max(M4_5HotPix);
[maxBP(15,1) maxBPI(15,1)] = max(M4_6HotPix);
[maxBP(16,1) maxBPI(16,1)] = max(M4_7HotPix);
[maxBP(17,1) maxBPI(17,1)] = max(M4_8HotPix);



     %%%%%%%%%%%%%%%%%%%%%%%%%%%%%%%%%%%%%%%%%%%%%%%%%%%%%%%%%%%%%%%%
  %% save bright pixel images

  C1numSlices = BPsaverMasked(C1HStack,[C1FileName(1:end-4) '_BP']);
  C2numSlices = BPsaverMasked(C2HStack,[C2FileName(1:end-4) '_BP']);
  C3numSlices = BPsaverMasked(C3HStack,[C3FileName(1:end-4) '_BP']);
  C4numSlices = BPsaverMasked(C4HStack,[C4FileName(1:end-4) '_BP']);

  M1_1numSlices = BPsaverMasked(M1_1HStack,[M1_1FileName(1:end-4)
'_BP']);

  M2_1numSlices = BPsaverMasked(M2_1HStack,[M2_1FileName(1:end-4)
'_BP']);
  M2_2numSlices = BPsaverMasked(M2_2HStack,[M2_2FileName(1:end-4)
'_BP']);
  M2_3numSlices = BPsaverMasked(M2_3HStack,[M2_3FileName(1:end-4)
'_BP']);

  M3_1numSlices = BPsaverMasked(M3_1HStack,[M3_1FileName(1:end-4)
'_BP']);

  M4_1numSlices = BPsaverMasked(M4_1HStack,[M4_1FileName(1:end-4)
'_BP']);
  M4_2numSlices = BPsaverMasked(M4_2HStack,[M4_2FileName(1:end-4)
'_BP']);
  M4_3numSlices = BPsaverMasked(M4_3HStack,[M4_3FileName(1:end-4)
'_BP']);
  M4_4numSlices = BPsaverMasked(M4_4HStack,[M4_4FileName(1:end-4)
'_BP']);
  M4_5numSlices = BPsaverMasked(M4_5HStack,[M4_5FileName(1:end-4)
'_BP']);
  M4_6numSlices = BPsaverMasked(M4_6HStack,[M4_6FileName(1:end-4)
'_BP']);
  M4_7numSlices = BPsaverMasked(M4_7HStack,[M4_7FileName(1:end-4)
'_BP']);
  M4_8numSlices = BPsaverMasked(M4_8HStack,[M4_8FileName(1:end-4)
'_BP']);
```

Subfunctions:

stackAnalysis_ctrl.m

```
%%%%%%%%%%%%%%%%%%%%%%%%%%%%%%%%%%%%%%%%%%%%%%%%%%%%%%%%%%%%%%%%%%%%%%%
%%%%
%%% stackAnalysis takes as inputs the stack name, the start image, and
the
%%% end image for a particular stack of combined confocal images.  It
%%% returns: the original stack as a structure, the cropped stack as a
%%% structure, the number of peaks in the hough transform, the crop
image,
%%% and the crop columns.  It also returns the average and peak
brightness
%%% of each slice, and the number of "bright" pixels, and the hough and
%%% bright pixel values normalized by the image size.
%%%
%%%
%%%
%%%%%%%%%%%%%%%%%%%%%%%%%%%%%%%%%%%%%%%%%%%%%%%%%%%%%%%%%%%%%%%%%%%%%%%
%%%%

function [AvgBrightness, PeakBrightness, HotPix, Pcts,
Peaks_norm,maskedStack,hotStack, NumPeaks, Peaks, Lines]...
     = stackAnalysis_ctrl(maskedStackName, ctrlBright)

houghThresh = .75;
%get hough outputs
[maskedStack, NumPeaks, Peaks, Lines] = ...
    stack_hough(maskedStackName, houghThresh);

%normalize hough outputs
pixSize = 2.259; %[um/pixel] pixel size in micrometers

ImArea = sum(sum(logical(maskedStack(:,:,1)))); %get image area
[pixels] excluding masked areas
ImArea_um = ImArea*pixSize^2; %get area in micrometers

Peaks_norm = (NumPeaks/ImArea_um)'; %[peaks/um^2] the number of peaks
per square micron

%get the "percent through thickness"
Ims =1:size(maskedStack,3);

Pcts = ((Ims-Ims(1))/(Ims(end)-Ims(1))*100)';

%open a file to write to
fileName = [maskedStackName(1:(end-4)), '_ctrl.csv'];
FID = fopen(fileName,'w');

Headers = ['NormThickness, AvgBrightness, PeakBrightness, PctBrightPix,
Peaks_norm\n'];
fprintf(FID,Headers);
%get average, peak brightness, and number of "bright" pixels
```

```
for i = 1:size(maskedStack,3)

    AvgBrightness(i,1) = maskedMean((maskedStack(:,:,i)));
    PeakBrightness(i,1) = max(max(maskedStack(:,:,i)));
    [HotPix(i,1) hotStack(:,:,i)] =
hotPixPct_ctrl(maskedStack(:,:,i),2.0,ctrlBright);
    currentLine = [num2str(Pcts(i)) ', ' num2str(AvgBrightness(i,1)) ',
'...
        num2str(PeakBrightness(i,1)) ', ' num2str(HotPix(i,1)) ', '
num2str(Peaks_norm(i,1)) '\n'];
    fprintf(FID,currentLine);

end

fclose(FID);
end
```

stack_hough.m

```
%%%%%%%%%%%%%%%%%%%%%%%%%%%%%%%%%%%%%%%%%%%%%%%%%%%%%%%%%%%%%%%%%%%%%%%%%
%%%%
%%% stack_hough takes as input the name of a series of grayscale tif
images per the
%%% convention used in stack_import, along with the start and stop
indices.
%%% Unlike older versions, this code does not use cropping, but uses
masked
%%% images as given out by Demo.m, using StackNStitch.
%%% The function gives as outputs the stack of
%%%  images as they were imported, the cropped stack, the original
stack as
%%%  imported, the number of peaks in the hough transform, the peaks,
the
%%%  lines associated with the peaks, and the image that shows how the
%%%  vessel images were cropped.
%%%
%%%
%%%
%%%%%%%%%%%%%%%%%%%%%%%%%%%%%%%%%%%%%%%%%%%%%%%%%%%%%%%%%%%%%%%%%%%%%%%%%
%%%%

function [maskedStack numPeaks peaks lines] = ...
    stack_hough(maskedStackName,Thresh)

isBW = true;


%first, import the stack of images:
maskedStack = cell2mat(struct2cell(load(maskedStackName))); %get the
output of the mat file as a single array


%now get the hough transform information for each image:
```

```
for imIndex = 1:size(maskedStack,3)
    %first do edge detection
    edgeStack(imIndex).img = edge(maskedStack(:,:,imIndex),'canny');

    [numPeaks(imIndex) peaks(imIndex).data lines(imIndex).data]...
        = hough_vessel(edgeStack(imIndex).img,Thresh,isBW);

    fprintf('image %d\n',imIndex);

end
```

hough_vessel.m

```
%%%%%%%%%%%%%%%%%%%%%%%%%%%%%%%%%%%%%%%%%%%%%%%%%%%%%%%%%%%%%%%%%%%%%%%%%
%%%%
%%% hough_vessel uses the hough function to find straight line segments
in
%%% a vessel image.  It takes as input a grayscale, binary, or color
image.
%%%  It returns as outputs the number of peaks in the hough transform
(that
%%%  is, the number of lines found in the image), the peak locations,
and
%%%  the line endpoints as output by the houghlines function
%%%
%%%
%%%%%%%%%%%%%%%%%%%%%%%%%%%%%%%%%%%%%%%%%%%%%%%%%%%%%%%%%%%%%%%%%%%%%%%%%
%%%%

function [numPeaks peaks lines] =
hough_vessel(vessel_image,Thresh,isBW)
if( nargin<3)
    Thresh = .75;
    isBW = false;
end
if isBW ==false
    image = rgb2gray(vessel_image);
else
    image = vessel_image;
end
%Performs a Hough analysis to find the number of lines in two images, a
%control and a damaged

%Perform hough transform on the images

[H, T, R] = hough(image);

%find the peaks in the hough transform
peaks = houghpeaks(H,10000,'Threshold',Thresh*max(H(:)));
```

```
lines = [];

%if there are lines to be found in the control image, find them...
if(~isempty(peaks))

    lines = houghlines(image,T,R,peaks,'FillGap',5,'MinLength',7);

end

numPeaks = length(lines);
```

maskedMean.m

```
%%%%%%%%%%%%%%%%%%%%%%%%%%%%%%%%%%%%%%%%%%%%%%%%%%%%%%%%%%%%%%%%%%%%%%%
%%%%
%%% maskedMean takes as an input a greyscale image, and outputs the
mean of all
%%% non-zero pixels
%%%
%%%
%%%%%%%%%%%%%%%%%%%%%%%%%%%%%%%%%%%%%%%%%%%%%%%%%%%%%%%%%%%%%%%%%%%%%%%
%%%%

function result = maskedMean(maskedIm)

[nRows nCols ~] = size(maskedIm);
vals = uint16([]);
for r = 1:nRows
    for c = 1:nCols

        if(uint16(maskedIm(r,c)>0))
            vals(end+1) = uint16(maskedIm(r,c));

        end

    end
end

result = mean(vals);



end
```

hotPixPct_ctrl.m

```
%%%%%%%%%%%%%%%%%%%%%%%%%%%%%%%%%%%%%%%%%%%%%%%%%%%%%%%%%%%%%%%%%%%%%%%
%%%%
%%%  hotPixPct_ctrl takes as input an image, and returns the percentage
of the
%%%  pixels in the image that are deemed "hot" checking if they are
more
%%%  than a user input factor above a control pixel brightness
%%%
%%%
%%%
%%%
%%%%%%%%%%%%%%%%%%%%%%%%%%%%%%%%%%%%%%%%%%%%%%%%%%%%%%%%%%%%%%%%%%%%%%%
%%%%

function [pctHot,hotPixImg] = hotPixPct_ctrl(img,factor,control)
%get the image size to begin with
[imRows imCols] = size(img);
hotPixImg = uint16(zeros(imRows,imCols));
numPix = sum(sum(logical(img)));

%look at each pixel, check if its brightness is within the margin

hotPixNum = 0;

for r =1:imRows
    for c = 1:imCols
        currentBrightness = img(r,c);
        if(currentBrightness>(factor*double(control)))
            hotPixNum = hotPixNum+1;
            hotPixImg(r,c) = img(r,c);
        end
    end
end

pctHot = hotPixNum/numPix*100;
```

StackNStitch.m

```
function Istitch = StackNStitch
%%
% This function reads in 'n' sequential z-stacks and stitches them side
by
% side (left to right). For each z-stack, the code places higher
integer
% images on top of lower integer images
%
% Assumptions
% 1) each stack has the same number of images
% 2) stacks are read in left-most first
% 3) each z-stack is stitched toward adventitia

%%
```

```
% Determine number of stacks
val = inputdlg('How many adjacent stacks do you want to stitch?');
n_stacks = str2double(val{1});

Istitch = []; % initialize stitched z-stacks
% For all n stacks
for i = 1:n_stacks
    % read in z-stack
    if i == 1
        [filename,pathname] = uigetfile('.tif','MultiSelect','On','Pick
all images in left-most stack');
        n_slices = length(filename);
    else
        [filename,pathname] =
uigetfile([pathname,'*.tif'],'MultiSelect','On',['Pick all images in
stack ',num2str(i),]);
        n_slices2 = length(filename);
        if n_slices2 ~= n_slices
            error('number of slices in stack has changed')
        end
    end
    % complile z-stack
    Istack = []; % initialize z-stack
    for j = 1:n_slices
        I = imread([pathname,filename{j}]);
        Istack = cat(3,Istack,I); % adds images toward adventitia
    end
    % stitch adjacent stack
    Istitch = cat(2,Istitch,Istack);
end
```

CreateMask.m

```
function [Imasked, Mask] = CreateMask(I)
% This function reads in a 2D or 3D grayscale image and walks the user
% through a series of steps to create a mask for that image. The first
step
% is to pick a threshold
%
% Inputs
% 1) I: a 2D or 3D array of uint12 integers (.mat)
%
% Outputs
% 1) Mask: a logical of the same size as I. Ones represent the pixels
% that should be masked out
% 2) Imasked: a matrix of the same size as I except masked values have
been set = 0
%

% Convert to double
I = double(I);

% Determine which slice in array is brightest
intensity = zeros(1,size(I,3));
```

```
for k = 1:length(intensity)
    intensity(k) = sum(sum(I(:,:,k)));
end
max_int = max(intensity);
k_max = find(intensity==max_int,1,'first');

% Select threshold of background
Slice = I(:,:,k_max);
Slice_thresh = Slice;
hist(Slice_thresh(:),100)
title('Select point such that vertical line divides background pixels')
xlabel('Pixel intensity')
ylabel('Frequency')
[thresh,dummy] = ginput(1); close all

% Set all background pixels equal to zero
Slice_thresh(Slice_thresh<thresh) = 1;
Slice_thresh(Slice_thresh>=thresh) = 0;
Mask1 = logical(Slice_thresh);

% Overlay slice with background
Slice_mask1 = Slice; Slice_mask1(Mask1) = 0;
SliceRGB = cat(3,Slice_mask1,Slice_mask1,Slice_mask1);
SliceRGB(Mask1) = 2^12-1;

% Allow user to outline additional bodies to add to mask
figure(1)
subplot(2,1,2)
imshow(uint16(Slice*2^4));
title('Original Image')
subplot(2,1,1)
imshow(uint16(SliceRGB*2^4));
title('Draw polygon to add to mask; double click; repeat; close fig
when done')
set(gcf,'units','normalized','outerposition',[0 0 1 1])
Mask2 = zeros(size(Slice));
set(gcf,'currentchar','c')          % set a dummy character
while get(gcf,'currentchar')=='c'   % which gets changed when key is
pressed
    BWi = roipoly;
    if ~isnan(BWi)
        Mask2 = Mask2 + double(BWi);
    end
end
close all

% Combine both masks
Mask = double(Mask1) + Mask2;
Mask(Mask>0) = 1;
Mask = logical(Mask);

% Add to border of mask (because difficult to select polygon at edge)
thickness = 10; % vary number of pixels to fill around border
top = Mask(thickness,:) == 1; % gaps in mask at top
Mask(1:thickness-1,top) = 1;
bottom = Mask(end-thickness,:) == 1; % gaps in mask at bottom
```

```
Mask(end-thickness:end,bottom) = 1;
left = Mask(:,thickness) == 1; % gaps in mask on left edge
Mask(left,1:thickness) = 1;
right = Mask(:,end-thickness) == 1; % gaps in mask on right edge
Mask(right,end-thickness:end) = 1;

% Display mask
Slice_mask = Slice; Slice_mask(Mask) = 0;
SliceRGB = cat(3,Slice_mask,Slice_mask,Slice_mask);
SliceRGB(Mask) = 2^12-1;
figure(2)
subplot(2,1,2)
imshow(uint16(Slice*2^4));
title('Original Image')
subplot(2,1,1)
imshow(uint16(SliceRGB*2^4));
title('Masked Image')

% Mask original matrix
Imasked = I;
for k = 1:size(I,3)
    slice_masked = Imasked(:,:,k);
    slice_masked(Mask) = 0;
    Imasked(:,:,k) = slice_masked;
end
```

BPSaverMasked.m

```
%%%%%%%%%%%%%%%%%%%%%%%%%%%%%%%%%%%%%%%%%%%%%%%%%%%%%%%%%%%%%%%%%%%%%%%%
%%%%
%%% BPsaverMasked takes as an input a stack of masked images in the
form of
%%% a 3D matrix, as well as a stack of images showing the bright pixels
%%% from the masked images. The function creates a single RGB image
stack
%%% with original images in grayscale, and the bright pixels in the
image
%%% highlighted in red.
%%%
%%%%%%%%%%%%%%%%%%%%%%%%%%%%%%%%%%%%%%%%%%%%%%%%%%%%%%%%%%%%%%%%%%%%%%%%
%%%%

function sliceNum = BPsaverMasked(maskedStack,saveName)



%create output imgs:
for sliceNum = 1:size(maskedStack,3)

    if(sliceNum<2)
        imwrite(maskedStack(:,:,sliceNum),[saveName '.tif']);
    else
        imwrite(maskedStack(:,:,sliceNum),[saveName
```

```
'.tif'],'WriteMode','append');
    end

end
% imshow(outputImg*2^4);



end
```

REFERENCES

1. Arribas, S.M., Daly, C.J., Gonzalez, M.C., McGrath, J.C., 2007. Imaging the vascular wall using confocal microscopy. Journal of Physiology 584, 5-9.

2. Austin, N., DiFrancesco, L.M., Herzog, W., 2010. Microstructural damage in arterial tissue exposed to repeated tensile strains. J Manipulative Physiol Ther 33, 14-19.

3. Baskaya, M.K., Rao, A.M., Dogan, A., Donaldson, D., Dempsey, R.J., 1997. The biphasic opening of the blood-brain barrier in the cortex and hippocampus after traumatic brain injury in rats. Neurosci Lett 226, 33-36.

4. Bell, E.D., Kunjir, R.S., Monson, K.L., 2013. Biaxial and failure properties of passive rat middle cerebral arteries. Journal of Biomechanics 46, 91-96.

5. Bell, E.D., Monson, K.L., 2013 Cerebrovascular dysfunction following sub-failure axial stretch. In ASME Summer Bioengineering Conference. Sunriver, Oregon.

6. Bell, E.D., Sullivan, J.W., Monson, K.L., 2015. Subfailure overstretch induces persistent changes in the passive mechanical response of cerebral arteries. Front Bioeng Biotechnol 3, 2.

7. Bouma, G.J., Muizelaar, P., 1990. Relationship between cardiac output and cerebral blood flow in patients with intact and with impaired autoregulation. J Neurosurg 73, 368-374.

8. Bouma, G.J., Muizelaar, P., Bandoh, K., Marmarou, A., 1992a. Blood pressure and intracranial pressure-volume dynamics in severe head injury: relationship with cerebral blood flow. J Neurosurg 77, 15-19.

9. Bouma, G.J., Muizelaar, P., Choi, S.C., Newlon, P.G., Young, H.F., 1991. Cerebral circulation and metabolism after severe traumatic brain injury: the elusive role of ischemia. J Neurosurg 75, 685-693.

10. Bouma, G.J., Muizelaar, P., Stringer, W.A., Choi, S.C., Fatouros, P., Young, H.F., 1992b. Ultra-early evaluationof regional cerebral blood flow in severely head-injured patients using xenon-enhanced computerized tomography. J Neurosurg 77, 360-368.

11. Bruce, D.A., Langfitt, T.W., Miller, J.D., Schutz, H., Vapalahti, M.P., Stanek, A.,

Goldberg, H.I., 1973. Regional cerebral blood flow, intracranial pressure, and brain metabolism in comatose patients. J Neurosurg 38, 131-144.

12. Burke, J.F., Stulc, J.L., Skolarus, L.E., Sears, E.D., Zahuranec, D.B., Morgenstern, L.B., 2013. Traumatic brain injury may be an independent risk factor for stroke. Neurology 81, 33-39.

13. Chan, P.D.S., Findlay, J.M., Vollrath, B., Cook, D.A., Grace, M., Chen, M.H., Ashforth, R.A., 1995. Pharmacological and morphological effects of in vitro transluminal balloon angioplasty on normal and vasospastic canine basilar arteries. J Neurosurg 83, 522-530.

14. Chen, Y.-H., Kang, J.H., Lin, H.-C., 2011. Patients With Traumatic Brain Injury: Population-Based Study Suggests Increased Risk of Stroke. Stroke 42, 2733-2739.

15. Chodobski, A., Zink, B.J., Szmydynger-Chodobska, J., 2011. Blood-brain barrier pathophysiology in traumatic brain injury. Transl Stroke Res 2, 492-516.

16. Cipolla, M.J., 2010. The Cerebral Circulation. Morgan & Claypool Lifesciences.

17. DeWitt, D.S., Prough, D.S., 2003. Traumatic Cerebral Vascular Injury: The Effects of Concussive Brain Injury on the Cerebral Vasculature. Journal of Neurotrauma 20, 795-825.

18. DeWitt, D.S., Prough, D.S., Deal, D.D., Vines, S.M., Hoen, H., 1996. Hypertonic saline does not improve cerebral oxygen delivery after head injury and mild hemorrhage in cats. Crit Care Med 24, 109-117.

19. DeWitt, D.S., Prough, D.S., Taylor, C.L., Whitley, J.M., Deal, D.D., Vines, S.M., 1992. Regional cerebrovascular responses to progressive hypotension after traumatic brain injury in cats. Am J Physiol 263, H1276-H1284.

20. DeWitt, D.S., Prough, D.S., Uchida, T., Deal, D.D., Vines, S.M., 1997. Effects of nalmefene, CG3703, tirilazad, or dopamine on cerebral blood flow, oxygen delivery, and electroencephalographic activity after traumatic brain injury and hemorrhage. J Neurotrauma 14, 931-941.

21. Dodds, S.D., Panjabi, M.M., Daigneault, J.P., 2004. Radiofrequency probe treatment for subfailure ligament injury: a biomechanical study of rabbit ACL. Clin Biomech (Bristol, Avon) 19, 175-183.

22. Eble, J.A., Niland, S., 2009. The extracellular matrix of blood vessels. Current Pharmaceutical Design 15, 1385-1400.

23. Ellis, E.F., Dodson, L.Y., Police, R.J., 1991. Restoration of cerebrovascular responsiveness to hyperventilation by the oxygen radical scavenger n-acetylcysteine

following experimental traumatic brain injury. J Neurosurg 75, 774-779.

24. Enevoldsen, E.M., Jensen, F.T., 1978. Autoregulation and CO2 responses of cerebral blood flow in patients with acute severe head injury. J Neurosurg 48, 689-703.

25. Engel, J., Bachinger, H.P., 2005. Structure, Stability and Folding of the Collagen Triple Helix, in: Brinckmann, J., Notbohm, H., Muller, P.K. (Eds.), Collagen. Springer-Verlag Berlin Heidelberg, pp. 7-33.

26. Engelborghs, K., Haseldonckx, M., van Reempts, J., van Rossem, K., Wouters, L., Borgers, M., Verlooy, J., 2000. Impaired autoregulation of cerebral blood flow in an experimental model of traumatic brain injury. J Neurotrauma 17, 667-677.

27. Faul, M., Xu, L., Wald, M.M., Coronado, V.G., 2010. Traumatic Brain Injury in the United States: Emergency Depatrment Visits, Hospitalizations and Deaths 2002-2006, in: Centers for Disease Control and Prevention, N.C.f.I.P.a.C. (Ed.), Atlanta, GA.

28. Fieschi, C., Beduschi, A., Agnoli, A., Battistini, N., Collice, M., Prencipe, M., Risso, M., 1972. Regional cerebral blood flow and intraventricular pressure in acute brain injuries. Europ Neurol 8, 192-199.

29. Finlay, H.M., McCullough, L., Canham, P.B., 1995. Three-Dimensional Collagen Organization of Human Brain Ateries at Different Transmural Pressures. Journal of Vascular Research 32, 301-312.

30. Finlay, H.M., Whittaker, P., Canham, P.B., 1998. Collagen organization in the branching region of human brain arteries. Stroke 29, 1595-1601.

31. Fonck, E., Prod'hom, G., Roy, S., Augsburger, L., Rufenacht, D.A., Stergiopulos, N., 2007. Effect of elastin degradation on carotid wall mechanics as assessed by a constituent-based biomechanical model. Am J Physiol Heart Circ Physiol 292, H2754-2763.

32. Fukuda, K., Tanno, H., Okimura, Y., Nakamura, M., Yamaura, A., 1995. The blood-brain barrier disruption to circulating proteins in the early period after fluid percussion brain injury in rats. J Neurotrauma 12, 315-324.

33. Holzapfel, G.A., Gasser, T.C., Ogden, R.W., 2000. A new constitutive framework for arterial wall mechanics and a comparitive study of material models. Journal of Elasticity 61, 1-48.

34. Humphrey, J.D., 1995. Mechanics of the Arterial Wall: Review and Directions. Crit Rev Biomed Eng 23, 1-162.

35. Jamal, A., Bendeck, M., Langille, B.L., 1992. Structural changes and recovery of function after arterial injury. Arteriosclerosis, Thrombosis, and Vascular Biology 12, 307-

317.

36. Jünger, E.C., Newell, D.A., Grant, G.A., Avellino, A.M., Ghatan, S., Douville, C.M., Lam, A.M., Aaslid, R., Winn, H.R., 1997. Cerebral autoregulation following minor head injury. J Neurosurg 86, 425-432.

37. Kelly, D.F., Martin, N.A., Kordestani, R., Counelis, G., Hovda, D.A., Bergsneider, M., McBride, D.Q., Shalmon, E., Herman, D., Becker, D.P., 1997. Cerebral blood flow as a predictor of outcome following traumatic brain injury. J Neurosurg 86, 633-641.

38. Lam, J.M.K., Hsiang, J.N.K., Poon, W.S., 1997. Monitoring of autoregulation using Doppler flowmetry in patients with head injury. J Neurosurg 86, 438-445.

39. Lewelt, W., Jenkins, L.W., Miller, J.D., 1980. Autoregulation of cerebral blood flow after experimental fluid percussion injury of the brain. J Neurosurg 53, 500-511.

40. Lewelt, W., Jenkins, L.W., Miller, J.D., 1982. Effects of experimental fluid-percussion injury of the brain on cerebrovascular reactivity to hypoxia and to hypercapnia. J Neurosurg 56, 332-338.

41. Li, Y., Foss, C.A., Summerfield, D.D., Doyle, J.J., Torok, C.M., Dietz, H.C., Pomper, M.G., Yu, S.M., 2012. Targeting collagen strands by photo-triggered triple-helix hybridization. Proceedings of the National Academy of Science 109, 14767-14772.

42. Li, Y., Ho, D., Meng, H., Chan, T.R., An, B., Yu, H., Brodsky, B., Jun, A.S., Yu, S.M., 2013. Direct Detection of Collagenous Proteins by Fluorescently Labeled Collagen Mimetic Peptides. Bioconjugate Chemistry 24, 9-16.

43. Li, Y., Yu, S.M., 2013. Targeting and mimicking collagens via triple helical peptide assembly. Current Opinion in Chemical Biology 17, 968-975.

44. Mizutani, T., Kojima, H., Asamoto, S., Miki, Y., 2001. Pathological mechanism and three-dimensional structure of cerebral dissecting aneurysms. J Neurosurg 94, 712-717.

45. Monson, K.L., Barbaro, N.M., Manley, G.T., 2008. Biaxial Response of Passive Human Cerebral Arteries. Annals of Biomedical Engineering 36, 2028-2041.

46. Muizelaar, J.P., Lutz III, H.A., Becker, D.P., 1984. Effect of mannitol on ICP and CBF and correlation with pressure autoregulation in severely head-injured patients. J Neurosurg 61, 700-706.

47. Munar, F., Ferrer, A.M., de Nadal, M., Poca, M.A., Pedraza, S., Sahuquillo, J., Garnacho, A., 2000. Cerebral hemodynamic effects of 7.2% hypertonic saline in patients with head injury and raised intracranial pressure. J Neurotrauma 17, 41-51.

48. Nawashiro, H., Shima, K., Chigasaki, H., 1995. Immediate cerebrovascular

responses to closed head injury in the rat. J Neurotrauma 12, 189-197.

49. Obrist, W.D., Langfitt, T.W., Jaggi, J.L., Cruz, J., Gennarelli, T.A., 1984. Cerebral blood flow and metabolism in comatose patients with acute head injury: Relationship to intracranial hypertension. J Neurosurg 61, 241-253.

50. Ohkawa, M., Fujiwara, N., Tanabe, M., Takashima, H., Satoh, K., Kojima, K., Irie, K., Honjo, Y., Nagao, S., 1996. Cerebral Vasospastic Vessels: Histologic Changes after Percutaneous Transluminal Angioplasty. Radiology 198, 179-184.

51. Overgaard, J., Tweed, W.A., 1974. Cerebral circulation after head injury. Part 1: Cerebral blood flow and its regulation after closed head injury with emphasis on clinical correlations. J Neurosurg 41, 531-541.

52. Povlishock, J.T., Becker, D.P., Sullivan, H.G., Miller, J.D., 1978. Vascular permeability alterations to horseradish peroxidase in experimental brain injury. Brain Res 153, 223-239.

53. Povlishock, J.T., Kontos, H.A., 1985. Continuing axonal and vascular change following experimental brain trauma. Cent Nerv Syst Trauma 2, 285-298.

54. Prat, R., Markiv, V., Dujovny, M., Misra, M., 1997. Evaluation of cerebral autoregulation following diffuse brain injury in rats. Neurol Res 19, 393-402.

55. Quinn, K.P., Lee, K.E., Ahaghotu, C.C., Winkelstein, B.A., 2007. Structural changes in the Cervical Facet Capsular Ligament: Potential contributions to Pain Following Subfailure Loading. Stapp Car Crash Journal 51, 169-187.

56. Quinn, K.P., Winkelstein, B.A., 2008. Altered collagen fiber kinematics define the onset of localized ligament damage during loading. J Appl Physiol (1985) 105, 1881-1888.

57. Rezakhaniha, R., Agianniotis, A., Schrauwen, J.T.C., Griffa, A., Sage, D., Bouten, C.V.C., van de Vosse, E.N., Unser, M., Stergiopulos, N., 2012. Experimental investigation of collagen waviness and orientation in the arterial adventitia using confocal laser scanning microscopy. Biomechanics and Modeling in Mechanobiology 11, 461-473.

58. Sacks, M.S., Schoen, F.J., 2002. Collagen fiber disruption occurs independent of calcification in clinically explanted bioprosthetic heart valves. J Biomed Mater Res 62, 359-371.

59. Schmidt, R.H., Grady, M.S., 1993. Regional patterns of blood-brain barrier breakdown following central and lateral fluid percussion injury in rodents. J Neurotrauma 10, 415-430.

60. Sellaro, T.L., Hildebrand, D., Lu, Q., Vyavahare, N., Scott, M., Sacks, M.S., 2007.

Effects of collagen fiber orientation on the response of biologically derived soft tissue biomaterials to cyclic loading. J Biomed Mater Res A 80, 194-205.

61. Suazo, J.A.C., Maas, A.I.R., van den Brink, W.A., van Santbrink, H., Steyerberg, E.W., Avezaat, C.J.J., 2000. CO2 reactivity and brani oxygen pressure monitoring in severe head injury. Crit Care Med 28, 3268-3274.

62. Tanno, H., Nockels, R.P., Pitts, L.H., Noble, L.J., 1992. Breakdown of the blood-brain barrier after fluid percussion brain injury in the rat: Part 2: Effect of hypoxia on permeability to plasma proteins. J Neurotrauma 9, 335-347.

63. Timmins, L.H., Wu, Q., Yeh, A.T., Moore, J.E., Jr., Greenwald, S.E., 2010. Structural inhomogeneity and fiber orientation in the inner arterial media. American Journal of Physiology-Heart and Circulatory Physiology 298, H1537-H1545.

64. Van Loon, P., Klip, W., Bradley, E.L., 1977. Length-force and volume-pressure relationships of arteries. Biorheology 14, 181-201.

65. Vaz, R., Sarmento, A., Borges, N., Cruz, C., Azevedo, T., 1998. Experimental traumatic cerebral contusion: morphological study of brain microvessels and characterization of the oedema. Acta Neurochir 140, 76-81.

66. Wan, W., Dixon, J.B., Gleason, R.L., Jr., 2012. Constitutive modeling of mouse carotid arteries using experimentally measured microstructural parameters. Biophys J 102, 2916-2925.

67. Wan, W., Yanagisawa, H., Gleason, R.L., Jr., 2010. Biomechanical and Microstructural Properties of Common Carotid Arteries from Fibulin-5 Null Mice. Annals of Biomedical Engineering 38, 3605-3617.

68. Wei, E.P., Dietrich, W.D., Povlishock, J.T., Navari, R.M., Kontos, H.A., 1980. Functional, morphological, and metabolic abnormalities of the cerebral microcirculation after concussive brain injury in cats. Circ Res 46, 37-47.

69. Whalen, M.J., Carlos, T.M., Kochanek, P.M., Clark, R.S.B., Heineman, S., Schiding, J.K., Franicola, D., Memarzadeh, F., Lo, W., Marion, D.W., Dekosky, S.T., 1999. Neutrophils do not mediate blood-brain barrier permeability early after controlled cortical impact in rats. J Neurotrauma 16, 583-594.

70. Wicker, B.K., Hutchens, H.P., Wu, Q., Yeh, A.T., Humphrey, J.D., 2008. Normal basilar artery structure and biaxial mechanical behaviour. Computer Methods in Biomechanics and Biomedical Engineering 11, 539-551.

71. Yamamoto, Y., Smith, R.R., Bernanke, D.H., 1992. Mechanism of Action of Balloon Angioplasty in Cerebral Vasospasm. Neurosurgery 30, 1-6.

72. Yamazoe, N., Hashimoto, N., Kikuchi, H., Kang, Y., Nakatani, H., Hazama, F., 1990. Study of the elastic skeleton of intracranial arteries in animal and human vessels by scanning electron microscopy. Stroke 21, 765-770.

73. Yu, S.M., Li, Y., Kim, D., 2011. Collagen mimetic peptides: progress towards functional applications. Soft Matter 7, 7927.